IVYSPRING INTERNATIONAL PUBLISHER

International Journal of Biological Sciences

2027; 23(1): 182-206. doi: 10.7150/ijbs.127457

Research Paper

tRNA-Derived Fragment tRF-1^{ArgACG} Drives HCC Osteolytic Bone Metastasis via ALKBH5-Mediated INPP4B Destabilization and PI3K/AKT Activation

Jinyan Feng[1*], Long Chen[1,4*], Xianfu Wei[1,3*], Houzhi Yang[1*], Xiuxin Han[1], Qingqian Zhao[1], Qian Li[1], Xin Chen[2], Chao Zhang[1], Yafei Wang[5✉], Bowen Liu[2✉], Guowen Wang[1✉]

1. National Key Laboratory of Druggability Evaluation and Systematic Translational Medicine, Tianjin's Clinical Research Center for Cancer, Department of Bone and Soft Tissue Tumors, Tianjin Medical University Cancer Institute and Hospital, National Clinical Research Center for Cancer, Tianjin, 300060, China.
2. Xinxiang Key Laboratory of Inflammation and Immunology, School of Medical Technology, Xinxiang Medical University, Xinxiang, Henan 453003, China.
3. Department of Orthopedics, Qilu Hospital of Shandong University, Jinan, Shandong, 250012, China.
4. Department of Musculoskeletal Oncology, Clinical Oncology School of Fujian Medical University, Fujian Cancer Hospital, Fuzhou 350000, China.
5. Department of Hematology, Tianjin Medical University Cancer Institute and Hospital, National Clinical Research Center for Cancer, Key Laboratory of Cancer Prevention and Therapy, Tianjin's Clinical Research Center for Cancer, Tianjin, 300060, China.

* Contributed equally to this work.

✉ Corresponding authors: Guowen Wang, E-mail: wangguowen@tmu.edu.cn; Bowen Liu, E-mail: liubowen309@163.com; Yafei Wang, E-mail: drwang2005@163.com, Department of Bone and Soft Tissue Tumors, Tianjin Medical University Cancer Institute and Hospital, Huanhu Xi Road, Tiyuan Bei, Hexi District, Tianjin 300060, P.R. China, Phone: +86-18802237773.

© The author(s). This is an open access article distributed under the terms of the Creative Commons Attribution License (https://creativecommons.org/licenses/by/4.0/). See https://ivyspring.com/terms for full terms and conditions.

Received: 2025.10.28; Accepted: 2026.10.12; Published: 2027.01.01

Abstract

The incidence of bone metastases in hepatocellular carcinoma (HCC) has risen significantly over the past decade, largely attributable to prolonged overall survival among HCC patients. Elucidating the molecular mechanisms underpinning HCC bone metastasis is thus imperative for developing effective preventive and therapeutic strategies. In this study, we identified a novel transfer RNA-derived fragment, tRF-1^{ArgACG}, which exhibited pronounced upregulation in HCC bone-metastatic tissues and was associated with shorter bone metastasis-free survival in HCC patients. Functionally, tRF-1^{ArgACG} facilitated HCC cell recruitment and adhesion to the osteoblastic niche through CXCR4/CXCL12 and CD44, and enhanced tumor growth within the bone microenvironment. Furthermore, tRF-1^{ArgACG} promoted osteoclastogenesis by increasing the RANKL/OPG ratio while suppressing osteoblast differentiation through DKK1 modulation, thereby disrupting bone homeostasis. Mechanistically, tRF-1^{ArgACG} directly bound to the m6A demethylase ALKBH5, augmenting its enzymatic activity and consequently enhancing m6A demethylation of INPP4B mRNA. This interaction specifically destabilized INPP4B mRNA in an m6A-YTHDF2-dependent manner, resulting in PI(3,4)P2 accumulation and PI3K/AKT activation, which further amplified downstream transcriptional programs promoting skeletal recruitment and disrupting bone homeostasis. Critically, the pro-metastatic effects driven by tRF-1^{ArgACG} overexpression were effectively reversed through targeted inhibition of tRF-1^{ArgACG}, ALKBH5 suppression, or pharmacologic blockade of the PI3K/AKT pathway using LY294002. These findings establish a role for tRF-1^{ArgACG} in disrupting bone homeostasis and illuminate key mechanisms driving HCC bone metastasis.

Keywords: tRNA-derived fragment, tRF-1^{ArgACG}, HCC bone metastasis, ALKBH5, INPP4B, PI3K/AKT

Introduction

Hepatocellular carcinoma (HCC), the sixth most common malignancy globally and the third leading cause of cancer mortality [1-4], presents significant therapeutic challenges. Prolonged overall survival (OS) of HCC patients has contributed to a marked rise in bone metastasis incidence over the past decade. As the second most frequent site of extrahepatic HCC spread, bone metastasis occurs in 25.4-37.09% of cases,

with a dismal 2-year survival rate below 5% [4-6]. HCC bone lesions are predominantly osteolytic, disrupting bone homeostasis *via* complex cellular crosstalk between tumor cells and bone matrix components [7-10]. This interaction establishes a bone metastatic niche where cancer-secreted molecules dysregulate the osteoclasts (OCs)-mediated resorption and osteoblasts (OBs)-mediated formation balance [11-14], initiating a feed-forward "vicious cycle" that drives uncontrolled tumor growth and pathological bone destruction. Central to this dysregulation is the RANKL/RANK/OPG axis: tumor- or bone-derived RANKL promotes OCs differentiation by binding RANK on pre-OCs, while osteoprotegerin (OPG) inhibits osteoclastogenesis by acting as a RANKL decoy receptor [15]. Despite clinical use of osteoclast-targeted agents like denosumab, which primarily alleviate metastatic progression without substantially improving survival [15-17], novel strategies targeting HCC bone metastasis pathogenesis remain critically needed.

Advances in genomic sequencing have identified tRNA-derived fragments (tRFs), a novel class of highly conserved small non-coding RNAs (14-35 nt) dysregulated in tumors and linked to malignancy [18-20]. Categorized into tRF-1, tRF-2, tRF-3, tRF-5, and i-tRF based on tRNA cleavage sites [21], tRFs show promise as therapeutic targets [18] and as high-abundance, stable diagnostic and prognostic biomarkers in biofluids [22, 23]. tRFs orchestrate multilevel gene regulation *via* several mechanisms: (i). tRFs interact with epigenetic modifiers such as DNMTs, HSPB1, and SETDB1 [24, 25], or modulate long terminal repeat (LTR) retrotransposon activity to influence gene expression [26]. (ii). tRFs recruit Argonaute proteins to form RNA-induced silencing complexes (RISCs) with target mRNA 3′UTRs [27], or competitively bind YBX1 to destabilize target mRNA transcripts [28]. (iii). tRFs interfere with translation initiation by displacing eIF4G from mRNA, thereby suppressing protein synthesis [29]. However, the mechanistic role of tRFs in HCC bone metastasis remains unexplored.

N6-methyladenosine (m6A) modification, a key post-transcriptional epigenetic regulator, influences mRNA processing, degradation, and translation, playing critical roles in normal physiological processes and tumorigenesis [30, 31]. AlkB homolog 5 (ALKBH5), an m6A demethylase, exhibits divergent or even opposing expression levels and functional impacts across different tumor types [32-35]. Mechanistically, ALKBH5 mediates its effects by demethylating m6A marks to weaken the recognition capabilities of "m6A-YTHDF2" or "m6A-IGF2BP" pathways, thereby stabilizing or destabilizing target mRNAs [30, 36]. Furthermore, emerging evidence indicates that non-coding RNAs interact with m6A-modifying enzymes, modulating their enzymatic activities to mediate m6A modifications and regulate downstream gene expression [37]. These findings underscore the complexity of m6A-dependent regulatory networks in tumorigenesis and highlight the therapeutic potential of targeting m6A-modifying enzymes and their interacting partners.

Inositol polyphosphate-4-phosphatase type II B (INPP4B), an inositol phosphatase cooperating with PTEN, dephosphorylates $PI(3,4)P_2$/$PI(3,4,5)P_3$ into $PI(3)P$/$PI(4,5)P_2$ to suppress AKT phosphorylation and inactivate the PI3K/AKT pathway, thereby serving as a tumor suppressor to inhibit oncogenic progression in malignancies including HCC, breast, and thyroid cancers [38, 39]. INPP4B accumulations and PI3K/AKT inactivation are reported as novel negative modulators of osteoclast differentiation and a prognostic locus for human osteoporosis [40]. Aberrant phosphorylation at Thr/Ser residues on AKT is central to pathway activation, and its dysregulation is closely associated with tumor progression [41, 42]. Moreover, it has been reported that the PI3K/AKT axis regulates bone metastasis-related genes through multiple coordinated pathways, including the master osteomimetic transcription factor RUNX2 [41, 43], bone homing-related genes such as CXCR4, BSP, and OSN [41, 44], and osteoclast differentiation regulators like RANKL, OPG, PTHrP, and ILs [45]. These findings underscore the critical role of INPP4B-mediated PI3K/AKT pathway inhibition in controlling oncogenic signaling and bone metastasis progression across multiple malignancies.

In this study, we found that tRF-1^{ArgACG} was significantly enriched in HCC bone-metastatic cells and tissues, and its overexpression correlated with shorter bone metastasis-free survival (BMFS) of HCC patients. tRF-1^{ArgACG} overexpression promoted HCC cell bone homing, induced bone metastatic niche formation and promoted osteolytic remodeling by disrupting bone homeostasis. Mechanistically, tRF-1^{ArgACG} interacted with ALKBH5 to enhance its demethylase activity, which further destabilized INPP4B mRNA in an m6A-YTHDF2-dependent manner, and consequently activated PI3K/AKT signaling. Downstream, RUNX2 regulated CXCR4 and RANKL expression, YBX1 promoted CD44 transcription, and β-catenin/TCF4 induced DKK1 expression, linking PI3K/AKT activation to skeletal recruitment and bone remodeling. Crucially, inhibition of tRF-1^{ArgACG}, suppression of ALKBH5, or pharmacologic PI3K/AKT blockade effectively reversed the pro-metastatic effects induced by tRF-1^{ArgACG} overexpression. These findings directly

implicate tRF-1^{ArgACG} in bone homeostasis dysregulation and elucidate key mechanisms underlying HCC bone metastasis.

Material and Methods

Patient samples

Clinical specimens originally obtained between 2005 and 2025 were retrieved from the institutional tissue biobank of Tianjin Medical University Cancer Institute and Hospital for the present study. The use of these archived specimens was approved by the Ethics Committee of Tianjin Medical University Cancer Institute and Hospital (Approval No. Ek2023114; March 3, 2023). The cohort comprised 84 HCC patients: 45 without bone metastasis and 39 with clinically confirmed bone metastasis. For patients without bone metastasis, paired primary tumor specimens and adjacent para-tumor liver tissues (n = 45 pairs) were obtained during hepatic resection. For patients with bone metastasis, primary HCC tissues were collected from 29 patients, and bone metastatic lesions were obtained from 21 patients. Among them, 11 patients provided matched primary HCC and bone metastatic tissues. Bone specimens were obtained during clinically indicated orthopedic procedures for pathological fractures, refractory cancer-related pain, or spinal/nerve compression. All tissues were first used for routine diagnostics, and only surplus material was allocated for research; all metastatic lesions were histopathologically confirmed. Each tissue was divided into two portions: one formalin-fixed and paraffin-embedded (FFPE) for histology, including H&E, immunohistochemistry (IHC), and *in situ* hybridization (ISH), and the other snap-frozen for RNA and protein analyses. Plasma samples were collected from 25 healthy donors, 36 HCC patients without bone metastasis, and 24 HCC patients with bone metastasis. All samples were processed following standardized protocols. Clinicopathological characteristics are summarized in Supplementary Table S1 and Table S2. For validation, a commercial tissue microarray (D760601, Bioaitech, Xi'an, China) containing 41 normal liver tissues and 35 HCC specimens (18 stage II, 15 stage IIIA, 2 stage IVA) was included. All procedures followed the Declaration of Helsinki, and appropriate written informed consent for the collection, storage, and research use of clinical specimens was obtained from the participants in accordance with institutional biobank procedures.

Animal experimental procedures

All animal experiments were performed using 5-week-old male BALB/c nude mice (SPF Biotechnology, Beijing, China) in accordance with institutional animal welfare regulations and were approved by the Animal Care Committee of Tianjin Medical University Cancer Institute and Hospital, China. Mice were randomly housed upon arrival. Blinding was applied during outcome assessment, and investigators performing BLI quantification, micro-CT measurements, and histopathological quantification were unaware of group allocation until the corresponding analyses were completed. Technical exclusion criteria included unsuccessful tumor-cell inoculation or technical failures that precluded reliable imaging or tissue analysis. Animals that were successfully inoculated but did not subsequently develop detectable bone metastasis were retained in the analyses. Animals were regularly monitored for body weight, mobility, access to food and water, general condition, and signs of pain or distress. Humane endpoints included >20% loss of baseline body weight, persistent inability to ambulate or access food or water, severe non-weight-bearing lameness, hindlimb paralysis, respiratory distress, ulceration, or persistent signs of pain or distress. Animals reaching any humane endpoint were euthanized immediately according to the institutionally approved procedure; all remaining animals were euthanized at the prespecified experimental endpoints.

Establishment of highly bone-metastatic HCC cell line

HCCLM3 cells stably expressing luciferase (3×10^5 cells in 200 μL PBS) were injected intracardially using a 29G syringe into male 5-week-old BALB/c nude mice (SPF Biotechnology, Beijing, China), following standard animal operating procedures and animal welfare regulations. Metastatic progression was monitored by bioluminescence imaging (BLI; IVIS Spectrum) after intraperitoneal administration of D-luciferin (75 mg/kg). Bone lesions were aseptically dissected from mice euthanized at 6 weeks, and tumor cells were isolated via enzymatic digestion using collagenase and hyaluronidase, then expanded in DMEM supplemented with puromycin. Sequential intracardiac reinjection and two rounds of *in vivo* selection yielded two highly bone-metastatic HCCLM3 sublines, designated HCCLM3-BM1 and HCCLM3-BM2. To compare bone-metastatic capacities, luciferase-labeled HCCLM3, HCCLM3-BM1, and HCCLM3-BM2 cells were separately inoculated into the left cardiac ventricle. Experimental groups were defined according to the tumor-cell population used for inoculation. Successful intracardiac inoculation was confirmed by immediate post-injection BLI, and eight mice with confirmed successful inoculation were included in each group (n = 8 per group). Metastatic dissemination was

monitored longitudinally by BLI. At the experimental endpoint, skeletal tissues were collected for micro-CT, H&E, and TRAP staining to evaluate osteolytic bone metastasis and associated bone remodeling.

tRFs and tiRNA sequencing

Total RNA was extracted from HCCLM3 and HCCLM3-BM2 cells using TRIeasy reagent (Yeasen, Shanghai, China). RNA integrity and concentration were assessed by agarose gel electrophoresis and a Nanodrop™ spectrophotometer. To remove RNA modifications that could interfere with library construction, RNA samples underwent the following pretreatments: 3′-aminoacyl deacylation to generate 3′-OH for 3′-adaptor ligation, 3′-cP (2′,3′-cyclic phosphate) removal to 3′-OH, 5′-OH phosphorylation to 5′-P for 5′-adaptor ligation, and m^1A and m^3C demethylation to enhance reverse transcription efficiency. Sequencing library construction and data acquisition were performed by Aksomics Inc. (Shanghai, China). Libraries were size-selected based on RNA biotypes and sequenced on an Illumina NextSeq 500 platform (Illumina, CA, USA) using 50 bp single-end reads.

Real-time quantitative PCR of tRFs (tRF-qPCR)

For tRF analysis, RNA modifications interfering with small RNA cDNA synthesis were removed using the rtStar™ tRF & tiRNA Pretreatment Kit (AS-FS-005, Arraystar Inc., Rockville, MD, USA). These modifications include terminal modifications blocking adaptor ligation and internal methylations. cDNA libraries were then generated using the rtStar™ First-Strand cDNA Synthesis Kit (AS-FS-003, Arraystar Inc., Rockville, MD, USA) through sequential ligation of a 3′-adaptor (5′-end to RNA 3′-end) and a 5′-adaptor (3′-end to RNA 5′-end), with non-ligated ends chemically blocked. The 3′-adaptor incorporates a universal reverse transcription primer site, minimizing adaptor-dimer formation while enhancing yield. RT-qPCR was performed using the 2^−ΔΔCt method, with U6 serving as the internal control. Primer sequences are provided in Supplementary Table S3.

Transwell migration assays

Osteoprogenitor cells (Pre-OBs) or Beas-2B cells were plated in the lower chamber of 24-well Transwell inserts (Corning, USA) and cultured to approximately 80% confluence in complete medium. HCC cells (5×10^4 cells per well) suspended in serum-free medium were added to the upper chamber. Cells were incubated at 37 °C in a humidified 5% CO_2 incubator for 24 h. Non-migrated cells on the upper membrane surface were removed, while migrated cells on the lower surface were fixed with 4% paraformaldehyde for 20 min and stained with 0.5% crystal violet for 15 min in the dark. Stained cells were imaged and quantified under bright-field microscopy.

Adhesion assay

Pre-OBs or Beas-2B cells were seeded into 24-well plates and cultured in complete medium until reaching full confluence. Subsequently, 5×10^4 HCC cells transfected with GFP-tagged plasmids were added to the pre-cultured wells and co-incubated for 30 min to allow adhesion. After incubation, wells were gently washed three times with PBS to remove non-adherent cells. The adhered HCC cells were observed and quantified using a fluorescence microscope. Adhesion efficiency was calculated as the ratio of adherent cancer cells to the initial number of cells introduced, expressed as a percentage.

Osteoclastogenesis assay

Bone marrow-derived macrophages (BMDMs) were aseptically isolated from the femurs and tibias of 8-week-old C57BL/6 mice. After dissection and soft tissue removal, the marrow was flushed with α-MEM and collected. Isolated BMDMs were initially cultured in α-MEM containing 40 ng/mL M-CSF (HY-P7050A, MedChem Express, USA) for 24 h. Non-adherent cells were collected and seeded into 24-well plates, then cultured for 6 days in α-MEM supplemented with M-CSF, RANKL, and HCC cell-conditioned medium (CM), with medium replaced every 48 h. On day 6, pre-osteoclasts (pre-OCs) were fixed with 4% paraformaldehyde/PBS (pH 7.4) and assessed for tartrate-resistant acid phosphatase (TRAP) expression using a commercial kit (AMK1002-005, Hangzhou, China). TRAP-positive multinucleated cells (> 3 nuclei) were defined as osteoclasts (OCs). For F-actin ring analysis, pre-OCs were stained with rhodamine-labeled phalloidin (ab176753, Abcam, USA) at room temperature for 60 min, counterstained with DAPI (S7113, Sigma-Aldrich, Germany), and visualized using a fluorescence microscope (Olympus). F-actin ring formation was quantified using ImageJ software.

Osteoblastogenesis assay: Pre-OBs were seeded into 24-well plates and cultured in osteogenic medium containing HCC cell CM, which was replenished every 48 h. Alkaline phosphatase (ALP) activity was assessed on day 14 using a TRAP/ALP Stain Kit (294-67001, Wako, Japan). Cells were fixed in pre-cooled fixative for 30 min, incubated with ALP substrate solution at room temperature in the dark for 15-45 min, rinsed with distilled water, and imaged under bright-field microscopy. ALP activity was quantified by measuring absorbance at 405 nm using a microplate reader according to the manufacturer's instructions.

Mineralization was evaluated by Alizarin Red S (ARS) staining (A5533, Sigma-Aldrich, Germany). Cells were fixed in cold 4% paraformaldehyde/PBS (pH 7.4) for 30 min, washed with distilled water, and incubated with ARS solution for 30 min in the dark. Absorbance was measured at 495 nm spectrophotometrically as specified by the manufacturer.

Intracardiac injection of HCC bone metastasis mice model

Male BALB/c nude mice were used to evaluate the role of tRF-1^{ArgACG} and the ALKBH5/INPP4B/PI3K/AKT axis in HCC bone metastasis *in vivo*. Luciferase-labeled HCC cells (3×10^5 cells in 200 μL PBS) were injected into the left cardiac ventricle. Successful intracardiac inoculation was confirmed by immediate post-injection BLI, and 10 mice with confirmed successful inoculation were included in each experimental group (n = 10 per group). (1) tRF-1^{ArgACG} overexpression: Luciferase-labeled HCCLM3 cells expressing tRF-1^{ArgACG} or the corresponding negative control were inoculated into the respective predefined groups. (2) tRF-1^{ArgACG} inhibition: Following successful intracardiac inoculation of luciferase-labeled HCCLM3-BM2 cells, mice were randomly allocated to the AgoInhibitor or Ago-NC treatment groups using a random-number table. Treatment was initiated on day 10, with AgoInhibitor or Ago-NC (RiboBio, Guangzhou, China) administered intravenously at 50 nmol twice weekly for 6 weeks. (3) Mechanistic validation: Mice were allocated to five groups: tRF-NC + vehicle, tRF-1^{ArgACG} + vehicle, tRF-1^{ArgACG} + IOX1, tRF-1^{ArgACG} + INPP4B KD + IOX1, and tRF-1^{ArgACG} + IOX1 + LY294002. Groups were predefined according to the tumor-cell population used for intracardiac inoculation and the corresponding treatment regimen. The corresponding luciferase-labeled HCCLM3 cells were inoculated on day 0, and pharmacological treatment was initiated on day 10. IOX1 (MedChemExpress, HY-12304) was administered orally at 15 mg/kg for 3 consecutive days per cycle for seven cycles, whereas LY294002 (MedChemExpress, HY-10108) was administered intravenously at 50 mg/kg twice weekly for 6 weeks. Metastatic progression was monitored longitudinally by BLI using an IVIS Spectrum system. Mice were euthanized at the scheduled endpoint on day 60 unless a humane endpoint was reached earlier. Hindlimb bones were collected for micro-CT, H&E, IHC, and TRAP analyses; lungs were collected for H&E assessment of metastatic burden; and blood samples were obtained for measurement of bone formation and resorption markers.

Intratibial injection of HCC bone metastasis mice model

5-week-old male BALB/c nude mice were inoculated with luciferase-labeled HCCLM3-BM2 cells (2.5×10^5 cells in 25 μL PBS) into the bone marrow cavity of the right tibia using a 27-gauge needle. Mice were randomly allocated using a random-number table before treatment initiation (n = 6 per group). At 2 weeks after tumor-cell inoculation, mice subsequently received AgoInhibitor or Ago-NC (RiboBio, Guangzhou, China) by intratibial injection at 5 nmol every 3 days for 2 weeks. Tumor progression and osteolytic changes were evaluated by BLI and micro-CT, respectively. At the scheduled experimental endpoint, mice were euthanized unless an earlier humane endpoint was reached. Hindlimb bones were harvested for micro-CT, H&E staining, TRAP staining, and IHC, and blood samples were collected for measurement of bone formation and resorption markers.

Micro-CT (μCT) analysis

The femur and tibia were isolated from euthanized mice and subsequently fixed in 4% paraformaldehyde solution. Using the Quantum GX μCT imaging system (PerkinElmer), the femur and tibia were scanned at a voltage of 60 kV and a pixel resolution of 8.8 μm. The scanned data was reconstructed using NRecon software (Bruker) to generate three-dimensional structures, enabling the calculation of bone microstructure parameters.

Statistical analysis: Statistical analyses were performed using GraphPad Prism 9.0 (GraphPad Software, San Diego, CA, USA). Data are presented as the mean ± SD unless otherwise indicated. Comparisons between two groups were performed using a two-tailed Student's *t*-test, and comparisons among multiple groups were performed using one-way or two-way ANOVA, as appropriate. Correlations between continuous variables were assessed using Pearson's correlation analysis. Survival curves were generated using the Kaplan–Meier method and compared using the log-rank test. All statistical tests were two-sided, and $P < 0.05$ was considered statistically significant. Statistical significance is indicated as $^*P < 0.05$, $^{**}P < 0.01$, and $^{***}P < 0.001$.

Results

tRNA-derived fragment tRF-1^{ArgACG} overexpression correlates with HCC bone metastasis

To investigate the mechanisms underlying HCC bone metastasis, we established highly bone-

metastatic HCCLM3 sublines (HCCLM3-BM1 and HCCLM3-BM2) through two rounds of intracardiac injection using a bone-metastatic mouse model **(Fig. S1A)**, as previously reported [46]. Intracardiac injection of these sublines into new cohorts of mice confirmed their bone-metastatic potential, as assessed by longitudinal bioluminescence imaging. The complete metastatic distribution of individual mice is summarized in **Table S4**. Analysis across anatomical sites showed that skeletal metastasis increased from 5/8 (62.5%) in parental HCCLM3 to 7/8 (87.5%) in both HCCLM3-BM1 and HCCLM3-BM2 groups. This increase was most evident in the limbs, where metastatic involvement progressively increased from 4/8 (50.0%) to 6/8 (75.0%) and 7/8 (87.5%), respectively, whereas skull/spinal involvement was observed in 3/8 (37.5%), 4/8 (50.0%), and 4/8 (50.0%) mice. In contrast, pulmonary metastasis decreased from 5/8 (62.5%) to 3/8 (37.5%) and 2/8 (25.0%), while liver/abdominal involvement did not increase during skeletal selection (4/8 (50.0%), 4/8 (50.0%), and 3/8 (37.5%), respectively) **(Fig. S1B)**. Longitudinal BLI further demonstrated greater limb metastatic burden in the bone-selected derivatives, particularly HCCLM3-BM2, together with shorter BMFS **(Fig. S1C, D)**. Consistent with these imaging findings, micro-CT and trabecular reconstruction showed more severe osteolytic destruction after skeletal selection, while H&E, TRAP, CTSK, and OCN analyses showed increased osteoclast activity accompanied by reduced OCN expression **(Fig. 1A and S1E–G)**. Furthermore, HCCLM3-BM1 and HCCLM3-BM2 cells exhibited enhanced migration toward pre-osteoblasts, with increased adhesion most evident in HCCLM3-BM2 cells **(Fig. S1H, I)**. Together, these findings confirm the enhanced bone-associated metastatic phenotype of the bone-selected HCCLM3 derivatives.

Furthermore, to identify and characterize the critical tRFs contributing to HCC bone metastasis, we compared tRFs expression profiles between HCCLM3 and HCCLM3-BM2 cells using tRF-seq. Comparative profiling identified 476 significantly dysregulated tRFs including 228 upregulated and 248 downregulated in HCCLM3-BM2 cells **(Fig. 1B, S2A and Table S5)**, while tRF-1 species were predominantly enriched **(Fig. S2B)**. Among the top five upregulated tRF-1 candidates **(Fig. S2C)**, tRF-1^{ArgACG} was selected for further investigation based on its marked enrichment in the bone-selected HCCLM3-BM1 and HCCLM3-BM2 cells, with the highest expression observed in HCCLM3-BM2 cells **(Fig. 1C and S2D)**. Fluorescence *in situ* hybridization (FISH) analysis confirmed tRF-1^{ArgACG} localization in both cytoplasm and nucleus **(Fig. S2E)**. To further evaluate the clinical relevance of tRF-1^{ArgACG} in HCC bone metastasis, we analyzed plasma and tissue cohorts with detailed clinicopathological information **(Tables S1 and S2)**. Plasma levels of tRF-1^{ArgACG} were significantly elevated in HCC patients with bone metastasis (n = 24) versus those without bone metastasis (n = 36) and healthy controls (n = 25) **(Fig. 1D)**, suggesting its potential as a bone metastasis-associated biomarker in HCC. Among 54 patients with evaluable bone turnover measurements, CTX was positively correlated with P1NP (R^2 = 0.170, P = 0.0019; **Fig. S3A**). Circulating tRF-1^{ArgACG} was positively associated with the bone-resorption marker CTX (R^2 = 0.1582, P = 0.0030; **Fig. S3B**), whereas no significant association was observed with the bone-formation marker P1NP (R^2 = 0.0017, P = 0.7681; **Fig. S3C**). Consistently, ISH revealed significantly higher tRF-1^{ArgACG} enrichment in HCC bone-metastatic lesions (n = 21) compared with primary HCC tissues from patients with (n = 29) or without bone metastasis (n = 45), and the lowest expression was observed in adjacent liver tissues (n = 45) **(Fig. 1E)**. Higher tRF-1^{ArgACG} expression was associated with reduced BMFS (n = 29; Log-rank *P* = 0.0102, **Fig. 1F**). In contrast, tRF-1^{ArgACG} expression showed no significant association with OS (n = 84; Log-rank *P* = 0.0747, **Fig. S2F**), suggesting a closer association with bone metastatic progression than with overall prognosis in HCC. To assess the potential influence of concomitant extraosseous metastases, we further performed site-stratified analyses in the plasma and tissue cohorts. Within either the non-BM or BM groups, tRF-1^{ArgACG} levels were not significantly associated with concomitant lung or other extraosseous metastases (all *P* > 0.05; **Fig. S3D, E, G–I**). Importantly, after excluding patients with any extraosseous metastasis other than bone, circulating and primary-tumor tRF-1^{ArgACG} remained significantly higher in patients with bone metastasis alone than in those without bone or other metastases (*P* = 0.0033 and *P* = 0.0243, respectively; **Fig. S3F, J**), supporting an association between elevated tRF-1^{ArgACG} and bone metastatic involvement. In addition, ISH on HCC tissue microarrays demonstrated increasing tRF-1^{ArgACG} expression with advancing clinical stage **(Fig. 1G)**. Collectively, these results indicate that tRF-1^{ArgACG} is significantly enriched in bone-metastatic HCC and is associated with shorter BMFS in patients.

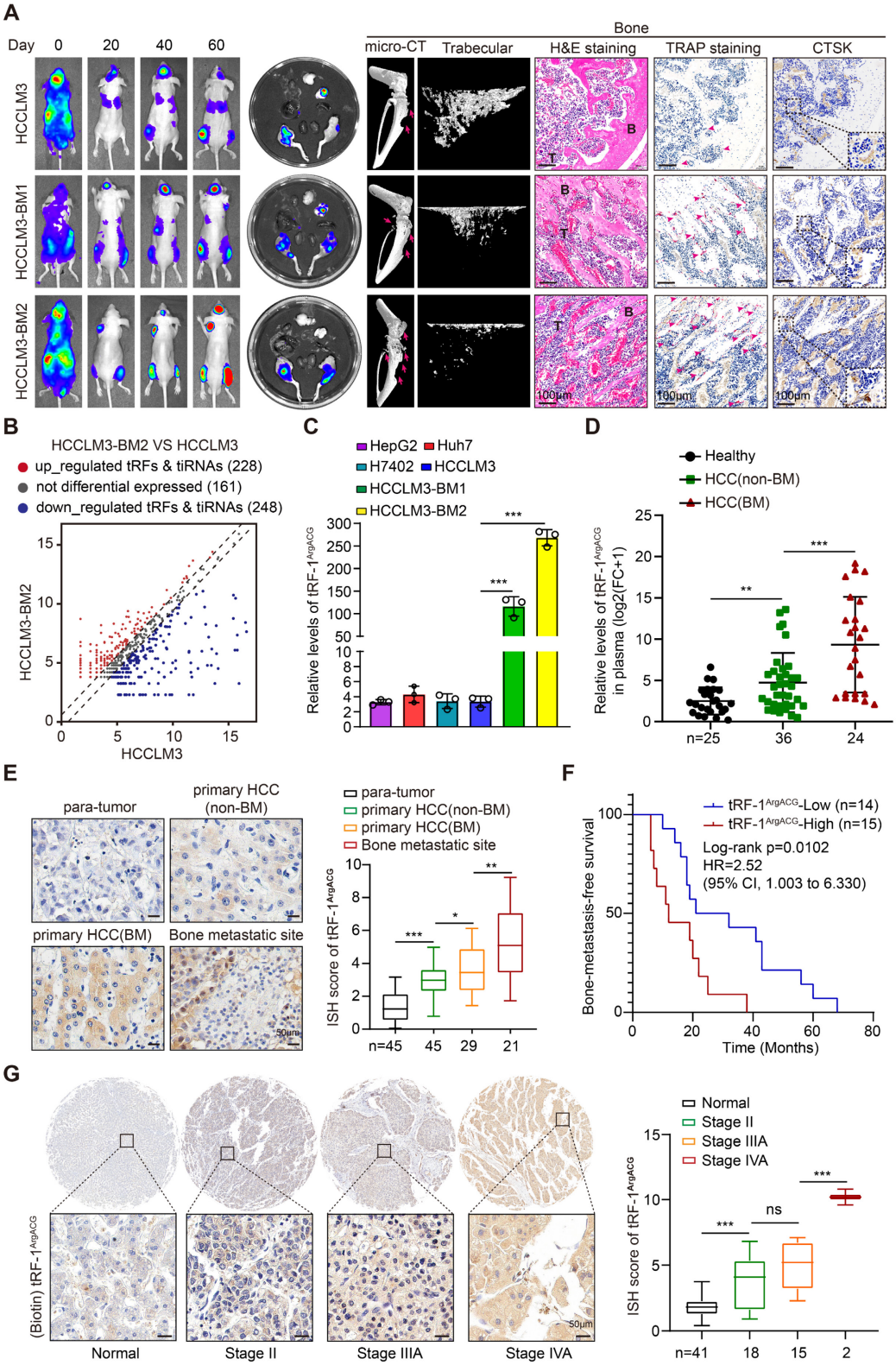


Figure 1. tRNA-derived fragment tRF-1^{ArgACG} overexpression correlates with HCC bone metastasis. (A) Representative longitudinal bioluminescence imaging (BLI) of mice after intracardiac injection of HCCLM3, HCCLM3-BM1, or HCCLM3-BM2 cells (n=8 successfully inoculated mice per group), together with *ex vivo* BLI of harvested bones and representative micro-CT, trabecular reconstruction, H&E staining, TRAP staining, and CTSK immunohistochemistry of bone lesions (T, tumor; B, bone; red arrows indicate osteolytic lesions or TRAP-positive osteoclasts, as indicated; scale bars = 100 μm). **(B)** Scatter plot of differentially expressed tRFs and tiRNAs between HCCLM3-BM2 and parental HCCLM3 cells. **(C)** tRF-qPCR analysis of tRF-1^{ArgACG} expression in HCC cell lines with varying metastatic potential. **(D)** Plasma tRF-1^{ArgACG} levels quantified *via* tRF-qPCR in healthy donors (n=25), HCC patients without bone metastasis (n=36), and HCC patients with bone metastasis (n=24). **(E)** tRF-1^{ArgACG} expression analyzed by ISH in para-tumor tissues (n=45), primary HCC without bone metastasis (n=45), primary HCC with bone metastasis (n=29), and bone-metastatic lesions (n=21; scale bars = 50 μm). **(F)** Kaplan–Meier analysis of bone metastasis-free survival (BMFS) in HCC patients stratified into high (n=15) and low (n=14) tRF-1^{ArgACG} expression groups using the cohort-specific median staining score of 3.46 as the cut-off (n=29; HR = 2.52, 95% CI: 1.003–6.330; log-rank *P* = 0.0102). **(G)** Representative ISH images (left) and quantification (right) of tRF-1^{ArgACG} expression in normal liver and HCC tissues across clinical stages on tissue microarrays (normal, n=41; stage II, n=18; stage IIIA, n=15; stage IVA, n=2; scale bars = 50 μm). Data are presented as mean ± SD where applicable. **P* < 0.05; ***P* < 0.01; ****P* < 0.001; ns, not significant.

tRF-1^{ArgACG} promotes HCC osteolytic bone metastasis *in vivo*

To evaluate the *in vivo* role of tRF-1^{ArgACG} in HCC bone metastasis, male nude mice were intracardially injected with luciferase-labeled HCCLM3 cells overexpressing tRF-1^{ArgACG} or control tRF-NC (**Fig. 2A and S4A**). BLI revealed that tRF-1^{ArgACG} overexpression accelerated skeletal colonization, with higher signal intensity and earlier onset of bone lesions compared with controls **(Fig. 2A-B)**. Consistently, Kaplan-Meier analysis demonstrated significantly shorter BMFS in tRF-1^{ArgACG}-bearing mice **(Fig. 2C)**. Skeletal metastasis was detected earlier in the tRF-1^{ArgACG}-overexpressing group, and the incidence of bone colonization reached 90% (9/10) by the experimental endpoint, compared with 40% (4/10) in the tRF-NC group **(Fig. 2C and S4B)**. Consistently, endpoint BLI demonstrated a markedly increased limb metastatic burden in mice bearing tRF-1^{ArgACG}-overexpressing tumors **(Fig. S4C)**. Histopathological analyses further supported these findings. TRAP-positive osteoclast numbers were markedly increased in tRF-1^{ArgACG}-overexpressing mice, accompanied by elevated CTSK expression and decreased OCN levels along the bone-tumor interface **(Fig. 2A, D)**. Micro-CT imaging confirmed aggravated bone destruction, with decreased BV/TV, Tb.N, and Tb.Th and increased Tb.Sp and BS/BV **(Fig. 2A, E)**, indicating that tRF-1^{ArgACG} promotes HCC osteolytic bone metastasis *in vivo*.

To assess the therapeutic potential of tRF-1^{ArgACG} inhibition, an optimized tRF-1^{ArgACG}-targeted inhibitor (AgoInhibitor) was administered intravenously in mice intracardially injected with HCCLM3-BM2 cells (**Fig. 2A and S4A**). Compared with Ago-NC-treated controls, AgoInhibitor markedly delayed the onset of skeletal metastases, reduced lesion intensity, and decreased the incidence of bone colonization from 70.0% (7/10) to 30.0% (3/10), with a corresponding reduction in limb metastatic BLI **(Fig. 2A-C and S4B, C)**. Histology demonstrated fewer TRAP+ osteoclasts, decreased CTSK expression, and increased OCN along the bone-tumor interface **(Fig. 2A, D)**. Micro-CT confirmed attenuation of osteolytic lesions, with increased BV/TV, Tb.N, and Tb.Th and decreased Tb.Sp and BS/BV **(Fig. 2A, E)**, suggesting that tRF-1^{ArgACG} inhibition suppresses skeletal metastatic progression and associated osteolysis. Consistently, in the intratibial model, AgoInhibitor treatment likewise reduced local tumor burden and mitigated osteolytic bone destruction, as evidenced by decreased tibial BLI intensity, improved trabecular parameters, fewer TRAP-positive osteoclasts, lower CTSK expression, and enhanced OCN staining **(Fig. S4D-F)**. In addition, AgoInhibitor treatment decreased serum CTX levels and increased P1NP levels **(Fig. S4G)**, consistent with reduced bone resorption and enhanced bone formation. Collectively, tRF-1^{ArgACG} promotes osteolytic bone metastasis in HCC, whereas its pharmacologic inhibition reduces skeletal metastatic burden and attenuates osteolytic bone destruction.

tRF-1^{ArgACG} facilitates HCC cell recruitment to osteoblasts and expansion in the bone microenvironment

To evaluate the role of tRF-1^{ArgACG} in facilitating HCC cell recruitment to the bone microenvironment, we overexpressed tRF-1^{ArgACG} in HepG2 and HCCLM3 cells, which exhibit relatively low endogenous levels, while HCCLM3-BM2 cells with high endogenous tRF-1^{ArgACG} expression were used for knockdown experiments. Overexpression and knockdown efficiency were confirmed *via* tRF-qPCR assays (**Fig. S5A**). Next, a transwell-based chemotaxis assay displayed that tRF-1^{ArgACG} depletion in HCCLM3-BM2 cells significantly impaired migration toward Pre-OBs, whereas its overexpression enhanced Pre-OB-directed migration in HepG2 and HCCLM3 cells **(Fig. 3A-B)**. *In vitro* adhesion assays further demonstrated that tRF-1^{ArgACG} knockdown attenuated HCCLM3-BM2 cell adhesion to Pre-OBs, whereas tRF-1^{ArgACG} overexpression enhanced the adhesion of HepG2 and HCCLM3 cells to Pre-OBs **(Fig. 3A, C)**. Together, these findings indicate that tRF-1^{ArgACG} promotes HCC cell recruitment to osteoblasts through enhanced directional migration and adhesion.

Given the osteoblast-mediated permissive microenvironment crucial for early metastatic establishment [47], we hypothesized that tRF-1^{ArgACG} elevation may also enhance the ability of HCC cells to expand within the bone microenvironment. We therefore used a bone-in-culture array (BICA) to assess HCC cell growth in an *ex vivo* bone microenvironment. Knockdown of tRF-1^{ArgACG} reduced the growth of HCCLM3-BM2 cells in bone cultures, whereas tRF-1^{ArgACG} overexpression significantly enhanced the growth of HepG2 and HCCLM3 cells **(Fig. 3D-E)**. Furthermore, colony formation assays showed that tRF-1^{ArgACG} depletion impaired, whereas its overexpression enhanced, the clonogenic growth of HCC cells in a Pre-OB-supported microenvironment **(Fig. S5B-C)**, supporting a role for tRF-1^{ArgACG} in promoting HCC cell growth within the bone microenvironment. To investigate the mechanisms underlying tRF-1^{ArgACG}-mediated HCC cell recruitment to bone, we first screened a panel of molecules implicated in tumor cell chemotaxis, adhesion, and interactions with the bone microenvironment (**Fig. S5D**).

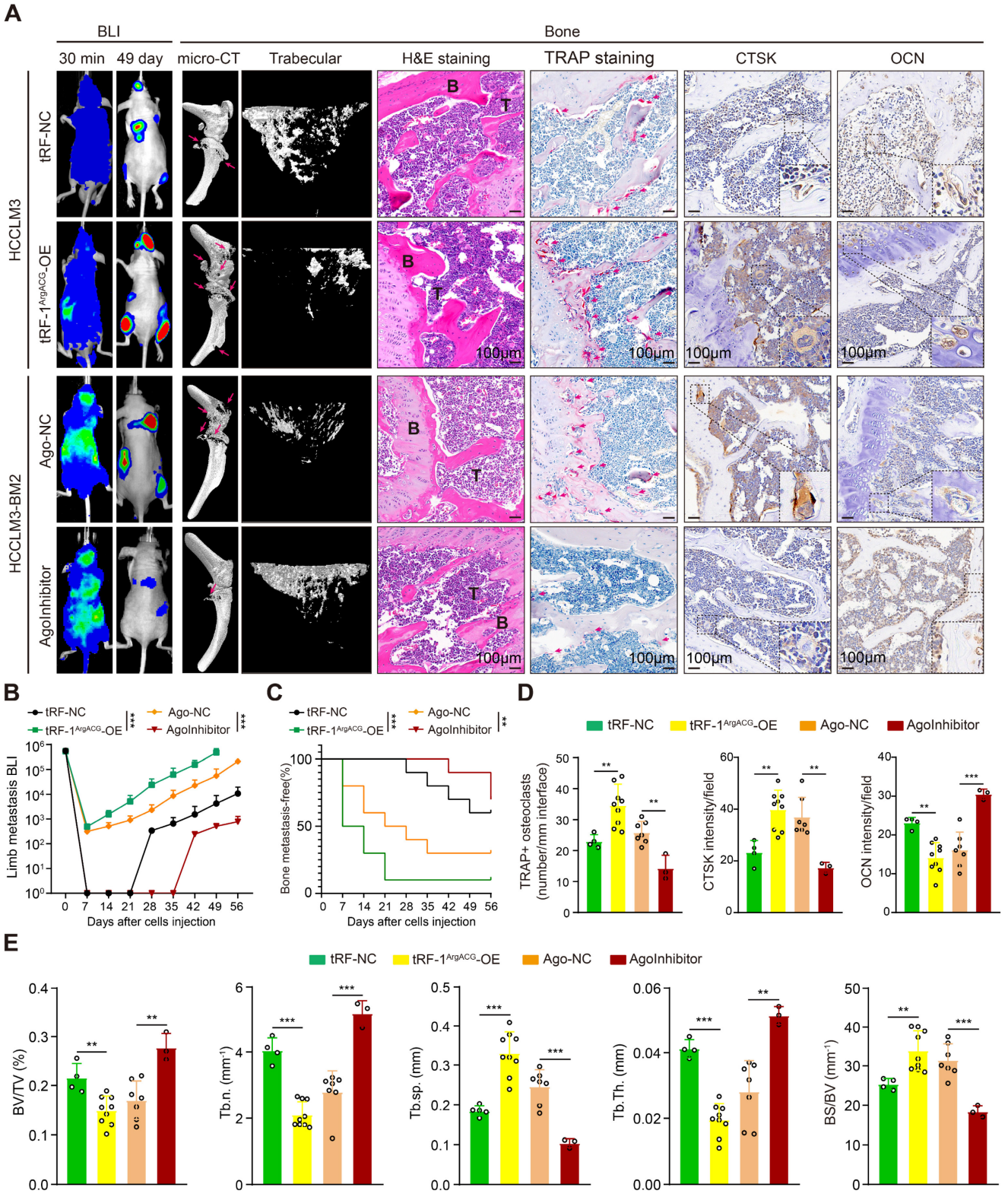


Figure 2. tRF-1^{ArgACG} promotes HCC osteolytic bone metastasis *in vivo*. (A) Representative BLI images at 30 min and 49 days after intracardiac inoculation, together with representative micro-CT, trabecular reconstruction, H&E, TRAP, CTSK, and OCN staining of bone lesions from the indicated mice (n=10 successfully inoculated mice per group). B, bone; T, tumor. Scale bars, 100 μm. **(B)** Longitudinal quantification of limb metastatic BLI signals in the indicated experimental groups following intracardiac inoculation. **(C)** Kaplan–Meier curves showing BMFS in the indicated experimental groups. **(D)** Quantification of TRAP-positive osteoclasts and CTSK and OCN staining in bone lesions from the indicated groups. **(E)** Quantitative micro-CT analysis of bone volume fraction (BV/TV), trabecular number (Tb.N), trabecular separation (Tb.Sp), trabecular thickness (Tb.Th), and bone surface-to-volume ratio (BS/BV). Data are presented as mean ± SD. Each data point represents one mouse. ***P*< 0.01; ****P*< 0.001.

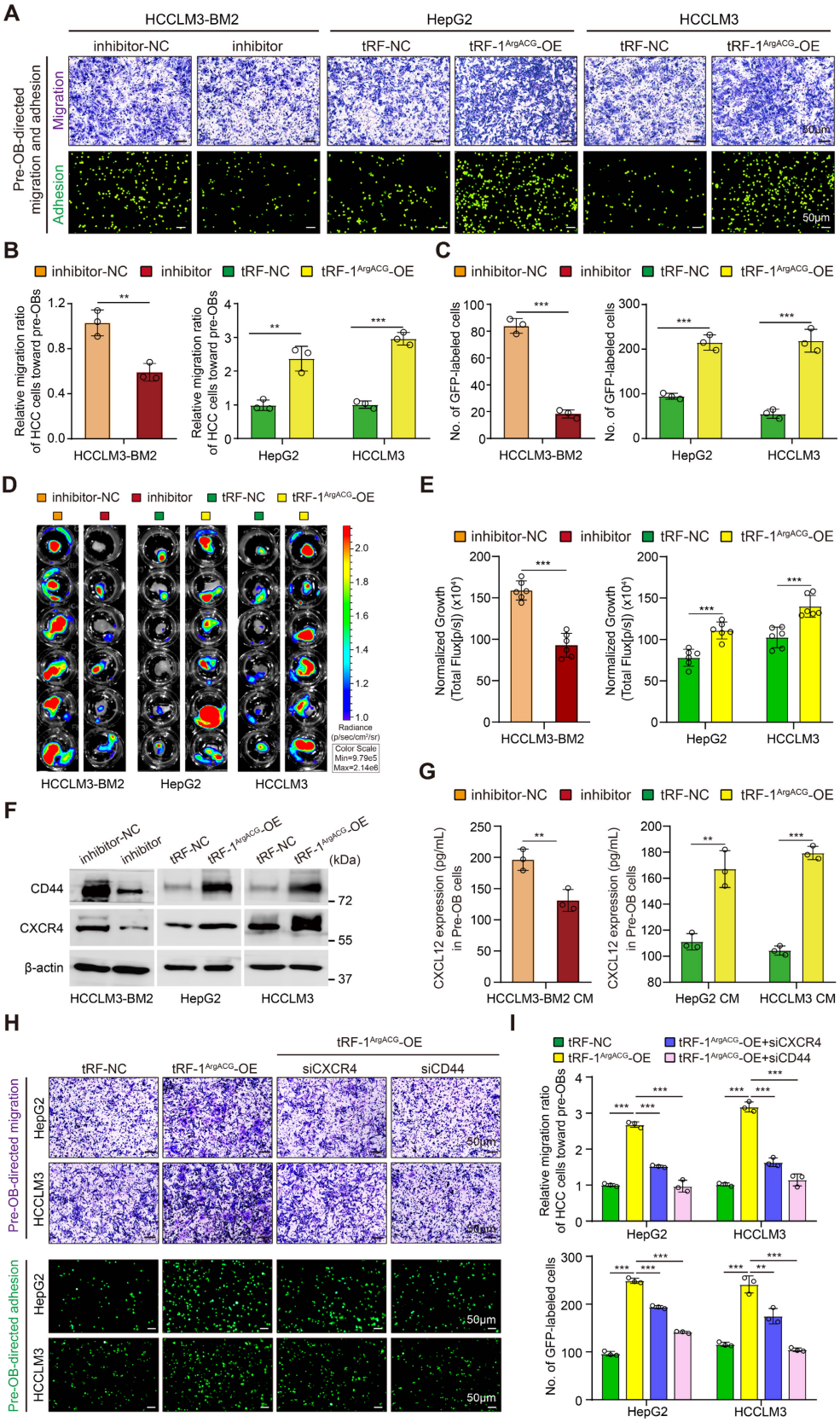


Figure 3. tRF-1^{ArgACG} facilitates HCC cell recruitment to osteoblasts and expansion in the bone microenvironment. (A–C) Representative images (A) and quantification (B, C) of Pre-OB-directed migration and adhesion assays in HCCLM3-BM2, HepG2, and HCCLM3 cells following tRF-1^{ArgACG} inhibition or overexpression, as indicated (scale bars = 50 μm). **(D, E)** Representative bioluminescence images (D) and quantification of total flux (E) showing the growth of luciferase-labeled HCC cells in the *ex vivo* bone-in-culture array (BICA) following tRF-1^{ArgACG} inhibition or overexpression. **(F)** Western blot analysis of CD44 and CXCR4 expression in HCCLM3-BM2, HepG2, and HCCLM3 cells following tRF-1^{ArgACG} inhibition or overexpression. **(G)** ELISA quantification of CXCL12 secretion by Pre-OBs following treatment with conditioned medium from tRF-1^{ArgACG}-modulated HCC cells. **(H, I)** Representative images (H) and quantification (I) of Pre-OB-directed migration and adhesion assays in HepG2 and HCCLM3 cells following tRF-1^{ArgACG} overexpression with or without CXCR4 or CD44 silencing (scale bars = 50 μm). Data are presented as mean ± SD. *P< 0.05; **P< 0.01; ***P< 0.001.

Among the candidates showing tRF-1^{ArgACG}-associated changes, CXCR4 and CD44 were prioritized for further functional investigation because of their established roles in directional chemotaxis and cell adhesion, respectively, which closely corresponded to the recruitment phenotypes observed above. Consistent with the screening results, tRF-1^{ArgACG} knockdown reduced CXCR4 and CD44 expression in HCCLM3-BM2 cells, whereas its overexpression increased their expression in HepG2 and HCCLM3 cells (**Fig. 3F**). We next examined several osteoblast-associated niche factors and observed tRF-1^{ArgACG}-associated changes in CXCL12, the major chemotactic ligand for CXCR4, in Pre-OBs exposed to HCC cell-conditioned medium **(Fig. S5E)**. We therefore further quantified CXCL12 levels in Pre-OBs by ELISA. Conditioned medium (CM) from tRF-1^{ArgACG}-silenced HCCLM3-BM2 cells decreased CXCL12 expression in Pre-OBs, whereas CM from tRF-1^{ArgACG}-overexpressing HepG2 and HCCLM3 cells increased CXCL12 levels **(Fig. 3G)**. Importantly, silencing either CXCR4 or CD44 significantly attenuated tRF-1^{ArgACG}-induced migration and adhesion toward Pre-OBs **(Fig. 3H, I)**. Collectively, these findings indicate that tRF-1^{ArgACG} promotes HCC cell recruitment and growth within the bone microenvironment, with CXCR4/CXCL12 and CD44 contributing to interactions with the osteoblastic niche.

tRF-1^{ArgACG} disrupts bone homeostasis by promoting osteoclastogenesis and suppressing osteoblastogenesis

Investigation of osteoblast-osteoclast bone homeostasis is crucial for understanding the vicious cycle of tumor progression and pathological bone destruction in HCC bone metastasis. Using C57BL/6 mice, we isolated BMDMs and BMSCs and induced them toward the osteoclast and osteoblast lineages, respectively **(Fig. S6A)**. First, we performed transwell chemotaxis assays to evaluate Pre-OC migration in response to CM from HCC cells with altered tRF-1^{ArgACG} expression. Overexpression of tRF-1^{ArgACG} in HepG2 and HCCLM3 cells significantly enhanced Pre-OCs migration, whereas knockdown of tRF-1^{ArgACG} in HCCLM3-BM2 cells markedly reduced it **(Fig. S6B-C)**, indicating that tRF-1^{ArgACG} modulates osteoclast precursor recruitment. We then examined chemokine signals implicated in osteoclast recruitment, focusing on CCL2, CCL5, and CX3CL1, which are known to regulate Pre-OCs chemotaxis and bone metastatic niche formation. tRF-1^{ArgACG} overexpression significantly upregulated CCL2 expression, whereas knockdown of tRF-1^{ArgACG} reduced its expression, while CCL5 and CX3CL1 levels remained largely unchanged **(Fig. S6D)**. Consistently, the receptor CCR2, but not CCR5, was markedly increased in Pre-OCs exposed to CM from tRF-1^{ArgACG}-overexpressing HCC cells, whereas CM from tRF-1^{ArgACG}-silenced cells decreased CCR2 levels **(Fig. S6E)**, supporting the involvement of the CCL2/CCR2 axis in tRF-1^{ArgACG}-mediated Pre-OC recruitment.

We next assessed osteoclast differentiation and maturation. CM from tRF-1^{ArgACG}-knockdown HCCLM3-BM2 cells significantly reduced TRAP+ cell formation compared with control CM, whereas CM from tRF-1^{ArgACG}-overexpressing HepG2 and HCCLM3 cells increased TRAP+ cells **(Fig. 4A-B)**. Similarly, actin ring-based podosome formation in Pre-OCs was impaired by CM from tRF-1^{ArgACG}-knockdown cells but enhanced by CM from overexpressing cells **(Fig. 4A-C)**, suggesting that tRF-1^{ArgACG} promotes Pre-OCs fusion and osteoclast maturation. Importantly, treatment with the CCL2 inhibitor Bindarit significantly attenuated osteoclast precursor migration induced by CM from tRF-1^{ArgACG}-overexpressing HCC cells. Moreover, Bindarit also reduced osteoclast differentiation, as indicated by decreased TRAP+ multinucleated cells, and impaired podosome formation as assessed by F-actin staining **(Fig. S7A-B)**, supporting the critical role of the CCL2/CCR2 axis in mediating tRF-1^{ArgACG}-driven osteoclastogenesis. We further examined the expression of osteoclastogenesis-related markers. Treatment with CM from tRF-1^{ArgACG}-knockdown HCCLM3-BM2 cells significantly downregulated *Ctsk*, *Nfatc1*, and *c-Fos* in Pre-OCs, whereas CM from tRF-1^{ArgACG}-overexpressing HCC cells markedly upregulated these markers **(Fig. 4D and S7C)**. We next examined the RANKL/OPG axis in HCC cells. RUNX2 and RANKL were reduced following tRF-1^{ArgACG} knockdown in HCCLM3-BM2 cells but increased following tRF-1^{ArgACG} overexpression in HepG2 and HCCLM3 cells, whereas OPG remained relatively unchanged **(Fig. 4E)**. Consistently, the RANKL/OPG ratio was decreased by tRF-1^{ArgACG} knockdown and increased by tRF-1^{ArgACG} overexpression **(Fig. S7D)**. In summary, these results indicate that tRF-1^{ArgACG} promotes osteoclastogenesis in HCC bone metastasis, in part through the CCL2/CCR2 axis and enhanced RANKL/OPG-mediated osteoclast activation.

Next, alkaline phosphatase (ALP) activity and alizarin red S (ARS)-stained mineralization assays revealed that CM from tRF-1^{ArgACG}-knockdown HCCLM3-BM2 cells significantly enhanced osteogenic differentiation, as evidenced by elevated ALP-positive pre-OBs, increased ALP activity, and augmented mineralized nodule formation relative to control CM. Conversely, CM from tRF-1^{ArgACG}-overexpressing HCC cells markedly suppressed these parameters

(**Fig. 4F-H**). Consistent with this, the expression of several osteoblastogenesis-related markers, including *OCN*, *Col-1a-1*, and *Osx*, was significantly up-regulated in pre-OBs treated with tRF-1^{ArgACG}-knockdown HCCLM3-BM2 CM, whereas tRF-1^{ArgACG}-overexpressing HCC CM downregulated their expression (**Fig. S7E**), indicating that tRF-1^{ArgACG} suppresses osteoblastogenesis in HCC bone metastasis. Given that DKK1 and Noggin are established extracellular modulators of osteoblast differentiation through antagonizing Wnt/β-catenin and BMP signaling, respectively [48, 49], we examined whether these osteogenic regulators were affected by tRF-1^{ArgACG}. DKK1 expression was decreased following tRF-1^{ArgACG} inhibition in HCCLM3-BM2 cells but increased following tRF-1^{ArgACG} overexpression in HepG2 and HCCLM3 cells, whereas Noggin remained largely unchanged **(Fig. S8A)**. Consistently, CM from tRF-1^{ArgACG}-overexpressing HCC cells decreased activating β-catenin phosphorylation at Ser552 in Pre-OBs, whereas CM from tRF-1^{ArgACG}-inhibited HCCLM3-BM2 cells increased p-β-catenin (S552), without appreciably affecting total β-catenin **(Fig. S8B)**. Importantly, DKK1 neutralization restored p-β-catenin (S552) levels and rescued the reductions in ALP activity and matrix mineralization induced by tRF-1^{ArgACG}-overexpressing HCC CM **(Fig. S8C and S8E-F)**. Conversely, recombinant human DKK1 (rhDKK1) reduced the elevated p-β-catenin (S552) levels and reversed the enhanced ALP activity and mineralization induced by CM from tRF-1^{ArgACG}-inhibited HCCLM3-BM2 cells **(Fig. S8D, G-H)**. These reciprocal rescue experiments support tumor-derived DKK1 as an important mediator of tRF-1^{ArgACG}-induced suppression of osteoblastogenesis. Collectively, these findings indicate that tRF-1^{ArgACG} disrupts bone homeostasis by promoting osteoclastogenesis and suppressing osteoblastogenesis.

tRF-1^{ArgACG}-induced INPP4B suppression and PI3K/AKT activation disrupt bone homeostasis in HCC

To further investigate the molecular mechanism underlying tRF-1^{ArgACG}-mediated disruption of bone homeostasis, we performed RNA-seq in HCCLM3 cells following tRF-1^{ArgACG} overexpression compared with negative controls **(Table S6)**. A volcano plot of the global differential expression profile identified 2,241 differentially expressed genes (DEGs), including 1,211 upregulated and 1,030 downregulated genes. Among the downregulated genes, INPP4B exhibited the largest fold change **(Fig. S9A)**. Functional enrichment analysis revealed enrichment of pathways related to oxidative phosphorylation, cell adhesion, and cytoskeletal organization **(Fig. S9B, C)**. Heatmap visualization of representative dysregulated genes and RT-qPCR validation further confirmed that INPP4B was markedly reduced following tRF-1^{ArgACG} overexpression **(Fig. 5A and S9D)**, prompting its selection for further mechanistic investigation. Validation experiments confirmed that tRF-1^{ArgACG} knockdown in HCCLM3-BM2 cells significantly upregulated INPP4B mRNA and protein levels, while its overexpression in HepG2 and HCCLM3 cells markedly decreased INPP4B **(Fig. 5B)**. Clinically, IHC analysis across HCC specimens revealed a gradient of decreasing INPP4B expression: highest in para-tumoral liver tissues (n=45), followed by primary HCC without (n=45) or with bone metastasis (n=29), and lowest in bone metastatic lesions (n=21) **(Fig. 5C-D)**. Kaplan–Meier analysis stratified by median INPP4B levels demonstrated that low INPP4B expression was significantly associated with reduced BMFS (n = 29; log-rank P = 0.0016; **Fig. 5E**) and OS (n = 84; log-rank P = 0.0042; **Fig. 5F**). Consistently, analysis of an independent HCC cohort showed that lower INPP4B expression was associated with shorter PFS (log-rank P = 0.00095; **Fig. S10A**). Importantly, Pearson correlation analysis indicated that INPP4B expression was negatively correlated with tRF-1^{ArgACG} levels (n=21, *P*=0.005; **Fig. S10B**).

We next conducted gain- and loss-of-function studies using lentiviral-mediated INPP4B knockdown or overexpression in HepG2/HCCLM3 and HCCLM3-BM2 cells, respectively, with confirmed transduction efficiency **(Fig. S10C)**. CM from INPP4B-depleted HepG2/HCCLM3 cells significantly enhanced pre-OCs fusion and maturation, evidenced by increased multinucleated TRAP+ OCs and F-actin ring formation, while impairing osteoblastogenesis as demonstrated by reduced ALP+ pre-OBs and ALP activity **(Fig. S10D)**. Conversely, CM from INPP4B-overexpressing HCCLM3-BM2 cells produced opposing effects **(Fig. S10E)**, consistent with a tumor-suppressive role for INPP4B in HCC bone metastasis. Mechanistically, INPP4B depletion substantially increased intracellular $PI(3,4)P_2$ levels and p-AKT in HepG2/HCCLM3 cells, whereas its overexpression reduced $PI(3,4)P_2$ accumulation and p-AKT in HCCLM3-BM2 cells, confirming INPP4B suppression-mediated PI3K/AKT activation *via* $PI(3,4)P_2$ **(Fig. S10F, G)**. We next performed rescue experiments to determine whether INPP4B mediates tRF-1^{ArgACG}-induced PI3K/AKT activation. tRF-1^{ArgACG} inhibition decreased intracellular $PI(3,4)P_2$ levels and AKT phosphorylation in HCCLM3-BM2 cells, both of which were partially restored by INPP4B silencing. Conversely, INPP4B restoration attenuated the increases in $PI(3,4)P_2$ and AKT phosphorylation

induced by tRF-1^{ArgACG} overexpression in HepG2 and HCCLM3 cells **(Fig. 5G, H)**. Critically, either restoring INPP4B or pharmacologically inhibiting PI3K/AKT with LY294002 attenuated the capacity of tRF-1^{ArgACG}-overexpressing HCC cells to promote osteoclastogenesis and reversed their inhibition of osteoblastogenesis **(Fig. 5I)**. These interventions also attenuated tRF-1^{ArgACG}-induced increases in the RANKL/OPG ratio and AKT phosphorylation in HCC cells, as well as the associated increase in CXCL12 levels in Pre-OBs **(Fig. S10H)**.

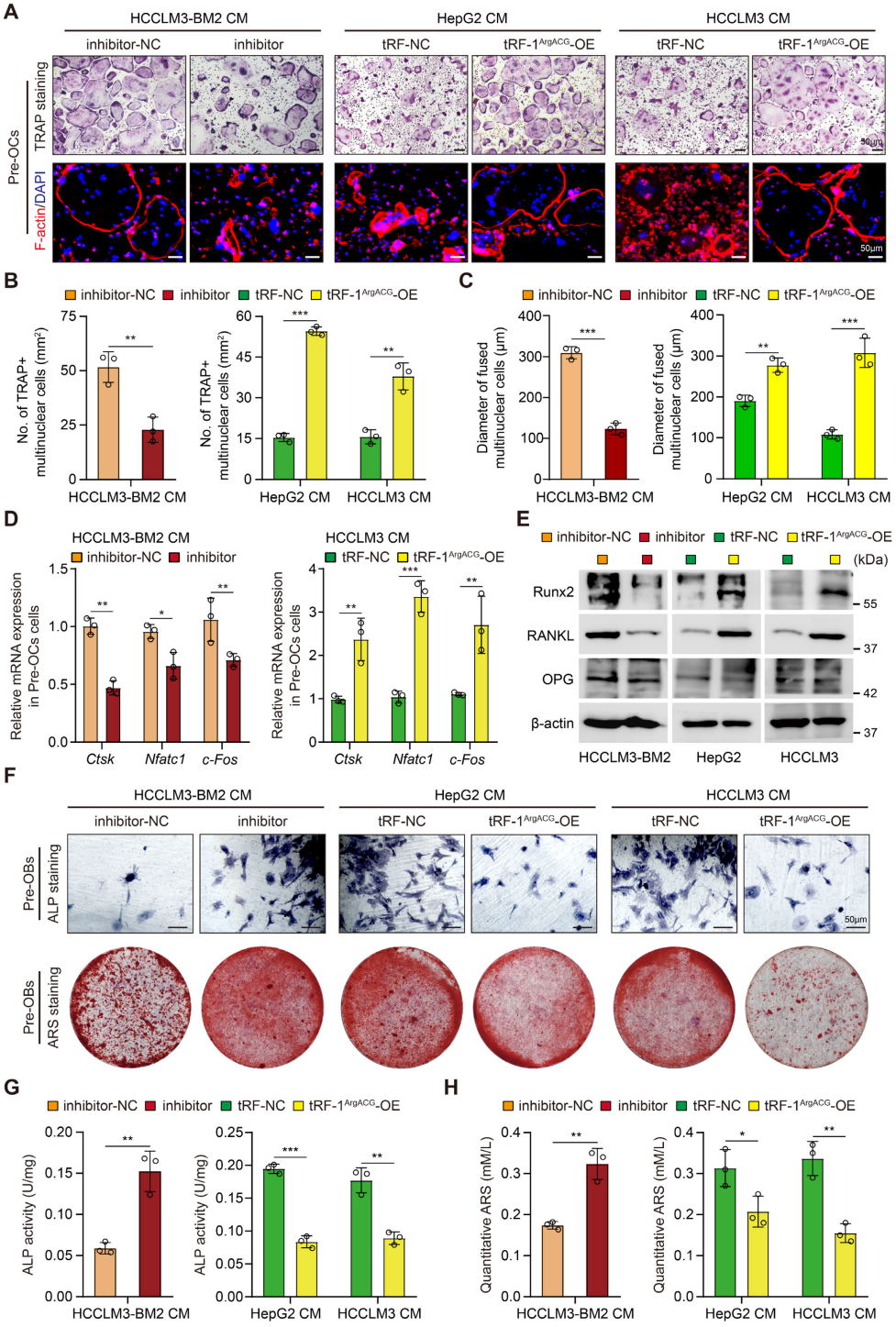


Figure 4. tRF-1^{ArgACG} enhances osteoclastogenesis but restrains osteoblastogenesis *in vitro*. **(A)** Osteoclastogenesis assay analyzed by TRAP staining (top) and IF staining of F-actin ring (bottom) in the presence of CM from tRF-1^{ArgACG}-inhibited or -overexpressing HCC cells. (Scale bars, 50 μm). **(B-C)** Quantification of TRAP-positive multinucleated cells (B) and the diameter of fused multinucleated cells (C); **(D)** RT-qPCR analysis of osteoclastogenesis marker mRNA levels, including *Ctsk*、*Nfatc1* and *C-fos*, in pre-OCs exposed to the indicated HCC CM. **(E)** Western blot analysis of RUNX2 and the osteoclastogenic regulators RANKL and OPG in tRF-1^{ArgACG}-modulated HCC cells. **(F)** osteoblastogenesis assay tested by ALP staining (top) or ARS staining (bottom) in the presence of CM from tRF-1^{ArgACG}-inhibited or -overexpressing HCC cells. (Scale bars, 50 μm). **(G-H)** quantification of ALP activity (G) and mineralization (H) in pre-OBs from the above experiment. Data represent mean ± SD of triplicate experiments. *P< 0.05; **P< 0.01; ***P< 0.001.

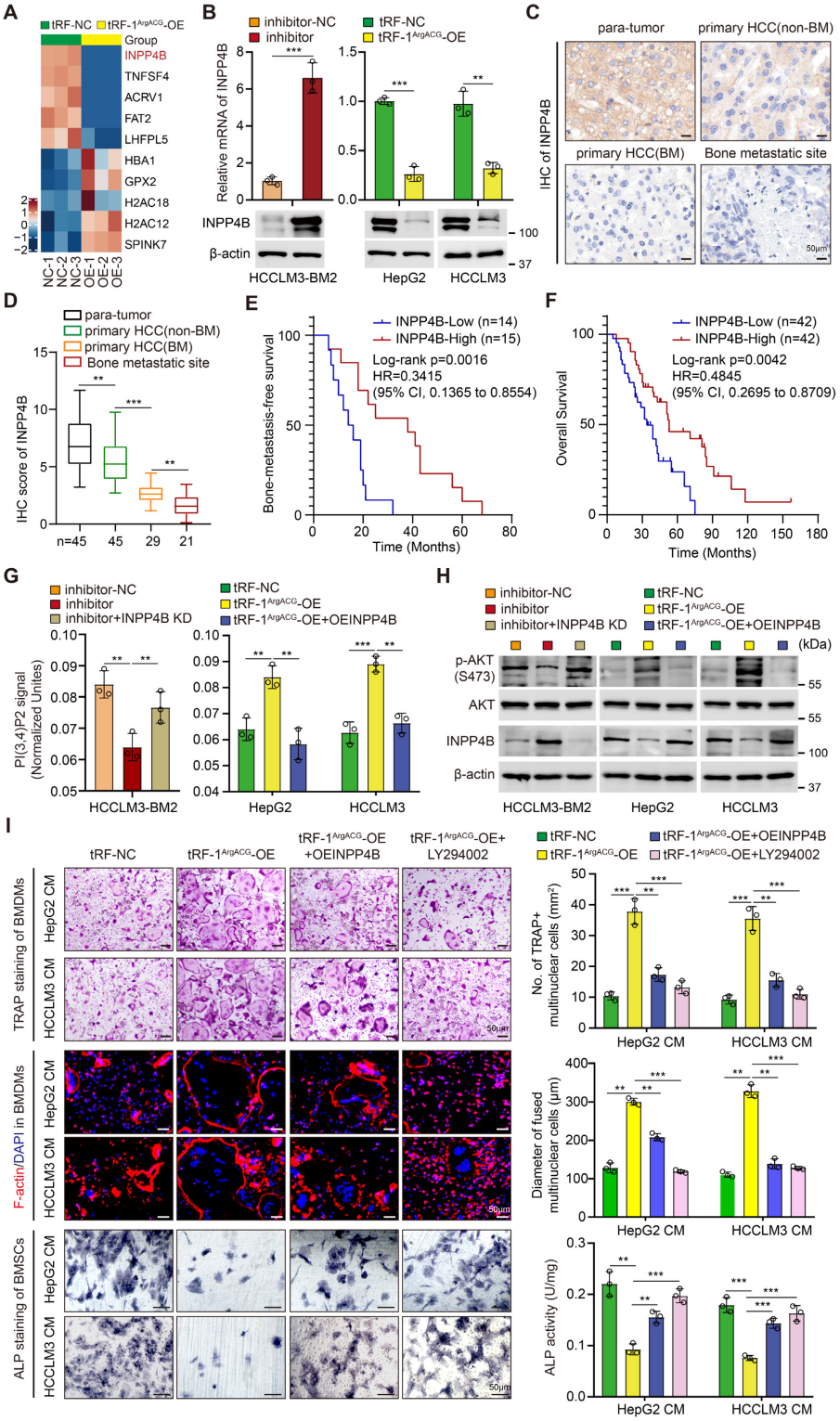


Figure 5. tRF-1^{ArgACG}-induced INPP4B suppression and PI3K/AKT activation disrupt bone homeostasis in HCC. (A) The heatmap displayed top 5 downregulated and 5 upregulated mRNAs identified by RNA-seq in HCCLM3/tRF-1^{ArgACG} compared to HCCLM3/tRF-NC cells. **(B)** RT-qPCR and Western blot assays assessing the mRNA and protein levels of INPP4B in HCC cells with tRF-1^{ArgACG} inhibition or overexpression. **(C-D)** Representative images of IHC staining (C) and quantification (D) of INPP4B expression in para-tumor tissues (n=45), primary HCC tissues without bone metastasis (n=45), primary HCC tissues with bone metastasis (n=29), and bone-metastatic lesions (n=21) (Scale bars, 50 μm). **(E)** Kaplan-Meier analysis of BMFS in HCC patients with high or low INPP4B expression levels in our clinical cohort using the cohort-specific median staining score of 2.61 as the cut-off (n=29; HR = 0.3415, 95% CI: 0.1365-0.8554, *P* = 0.0016; log-rank test). **(F)** Kaplan-Meier analysis of OS in HCC patients stratified by high or low INPP4B expression using our clinical cohort using the cohort-specific median staining score of 3.495 as the cut-off (n=84; HR = 0.4845, 95% CI: 0.2695-0.8709, *P* = 0.0042; log-rank test). **(G)** HCCLM3-BM2 cells were transduced with inhibitor-NC, inhibitor, and inhibitor combined with INPP4B knockdown; HepG2 and HCCLM3 cells were transfected with tRF-NC, tRF-1^{ArgACG}, tRF-1^{ArgACG} combined with INPP4B restoration. ELISA assays were used to determine the PI(3,4)P2 levels in the indicated HCC cells. **(H)** Western blot analysis of INPP4B, total AKT, and phosphorylated AKT (Ser473) in the indicated HCC cells as above. **(I)** HepG2 (top) and HCCLM3 (bottom) cells were treated with tRF-NC, tRF-1^{ArgACG}, and tRF-1^{ArgACG} combined with INPP4B restoration or LY294002 co-treatment. TRAP staining, F-actin ring formation and ALP staining assays were performed to evaluate osteoclastogenesis and osteoblastogenesis differences in the indicated HCC CM. Representative images (left) and quantification (right) are shown (scale bars, 50 μm). Data represent mean ± SD of triplicate experiments. **P*< 0.05; ***P*< 0.01; ****P*< 0.001.

To further define the transcriptional mechanisms linking PI3K/AKT activation to the bone-metastatic phenotype, we examined candidate transcriptional regulators of CXCR4, RANKL, CD44, and DKK1 based on previous evidence [50-54]. RUNX2 was prioritized as a common regulator of CXCR4 and RANKL. tRF-1^{ArgACG} overexpression increased RUNX2, CXCR4, and RANKL expression, whereas restoration of INPP4B or PI3K inhibition with LY294002 attenuated these effects **(Fig. S11A)**. RUNX2 depletion similarly reduced CXCR4 and RANKL expression and attenuated the tRF-1^{ArgACG}-induced increases in their promoter activities **(Fig. S11B, C and E)**. Consistently, ChIP-qPCR showed increased RUNX2 occupancy at the CXCR4 (−1555 to −1446 bp) and RANKL (−275 to −166 bp) regulatory regions following tRF-1^{ArgACG} overexpression **(Fig. S11D, F)**. We further examined YBX1 and β-catenin/TCF4 as candidate transcriptional regulators of CD44 and DKK1, respectively. tRF-1^{ArgACG} overexpression increased YBX1 phosphorylation and CD44 expression, whereas INPP4B restoration or LY294002 treatment attenuated these changes **(Fig. S11G)**. YBX1 depletion reduced CD44 expression and promoter activity, while ChIP-qPCR demonstrated increased YBX1 occupancy at the CD44 promoter (−1112 to −1012 bp) following tRF-1^{ArgACG} overexpression **(Fig. S11H-J)**. Similarly, tRF-1^{ArgACG}-induced DKK1 expression was attenuated by INPP4B restoration or LY294002 treatment **(Fig. S11K)**, whereas β-catenin depletion reduced DKK1 expression and promoter activity **(Fig. S11L, M)**. ChIP-qPCR further demonstrated increased TCF4 occupancy at the proximal DKK1 promoter (−121 to −37 bp) following tRF-1^{ArgACG} overexpression **(Fig. S11N)**. Together, these findings indicate that tRF-1^{ArgACG}-induced PI3K/AKT activation engages RUNX2, YBX1, and β-catenin/TCF4-dependent transcriptional programs to upregulate CXCR4/RANKL, CD44, and DKK1, respectively. Collectively, these findings indicate that the tRF-1^{ArgACG}–INPP4B–PI3K/AKT axis promotes HCC bone metastasis by coordinating tumor recruitment and bone homeostatic disruption through downstream transcriptional programs.

tRF-1^{ArgACG} suppresses INPP4B through enhancing ALKBH5 demethylase activity

We further explored the mechanism by which tRF-1^{ArgACG} suppressed INPP4B. Previous studies have shown that tRFs can regulate downstream targets through miRNA-like activity, translational control, or post-transcriptional modifications. Bioinformatic prediction by KangChen Bio-tech Inc indicated that INPP4B was not a direct miRNA-like target of tRF-1^{ArgACG} **(Table S7)**. To evaluate potential translational regulation, CHX chase assays demonstrated that modulation of tRF-1^{ArgACG} did not alter the half-life of INPP4B protein, indicating that INPP4B protein stability is unaffected **(Fig. S12A-C)**. Moreover, polysome profiling showed no significant changes in the distribution of INPP4B mRNA between monosome and polysome fractions upon tRF-1^{ArgACG} overexpression or knockdown **(Fig. S12D-I),** indicating that translation efficiency of INPP4B is not altered. To explore potential protein interactions, we performed RNA pull-down assays with biotinylated tRF-1^{ArgACG} followed by silver staining and observed an enriched protein band in the tRF-1^{ArgACG} pull-down fraction compared with the controls (**Fig. 6A**). Mass spectrometry identified ALKBH5, a key m6A demethylase in HCC, as the top candidate binding protein (**Fig. 6B, S13A and Table S8**). Further, RNA pull-down and western blot assays confirmed that tRF-1^{ArgACG} physically bound to ALKBH5 in HCC cells (**Fig. 6C, S13B**). Subsequent RIP-qPCR experiments revealed that the tRF-1^{ArgACG} precipitated by the ALKBH5 antibody was significantly more abundant than that in the IgG antibody group (**Fig. 6D, S13C**).

In addition, we performed computational docking analysis using the AlphaFold Server (https://alphafold.ebi.ac.uk/), which predicted a potential binding interface between tRF-1^{ArgACG} and ALKBH5, identifying U3 and U16 regions of tRF-1^{ArgACG} as key interaction sites forming hydrogen bonds or hydrophobic interactions with ALKBH5 residues, including Gln196, Arg130 and Cys200 (**Fig. S13D**). Moreover, FISH and IF co-localization experiments supported the interaction between tRF-1^{ArgACG} and ALKBH5 in HCC cells (**Fig. 6E, S13E**). Interestingly, modulating tRF-1^{ArgACG} levels did not alter ALKBH5 mRNA or protein expression (**Fig. S13F**). However, based on evidence that non-coding RNAs can allosterically activate ALKBH5 [55], we assessed its enzymatic activity. tRF-1^{ArgACG} overexpression increased ALKBH5 demethylase activity and reduced global m6A levels in HepG2 and HCCLM3 cells (**Fig. 6F**). Conversely, tRF-1^{ArgACG} depletion reduced ALKBH5 activity and increased m6A levels in HCCLM3-BM2 cells **(Fig. S13G)**, indicating that tRF-1^{ArgACG} binds to ALKBH5 and increases its demethylase activity. To further determine whether this interaction contributes to ALKBH5 activation, we generated U3A, U16A, and U3A/U16A mutants of tRF-1^{ArgACG} based on the docking-predicted interaction sites. RNA pull-down assays showed that the U3A mutation had little effect on ALKBH5 binding, whereas U16A markedly impaired the interaction, with the U3A/U16A double mutant showing a similarly pronounced reduction **(Fig. 6G)**. Consistent with the binding results, U3A

largely retained the ability of tRF-1^{ArgACG} to enhance ALKBH5 demethylase activity, whereas this effect was substantially attenuated by U16A and the U3A/U16A double mutation **(Fig. 6H)**. Correspondingly, m^{6}A dot blot analysis showed increased global m^{6}A levels predominantly in the U16A and U3A/U16A mutant groups **(Fig. 6H)**, suggesting that U16 is important for tRF-1^{ArgACG} binding to ALKBH5 and the resulting increase in its demethylase activity.

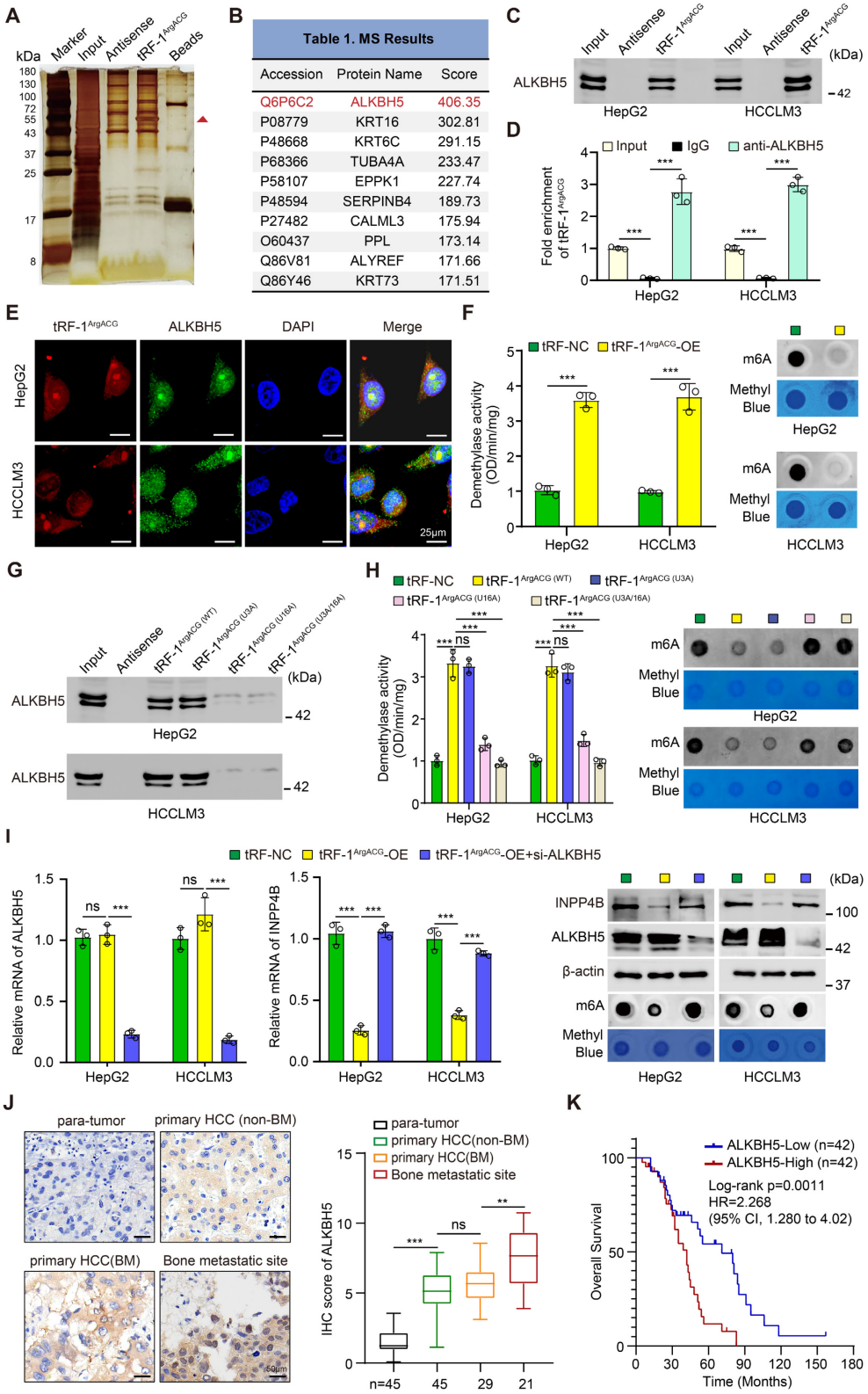


Figure 6. tRF-1^{ArgACG} functions through binding to the demethylase ALKBH5. (A) Silver SDS-PAGE gel showing proteins pulled down by biotin-labeled tRF-1^{ArgACG} or antisense in HCCLM3-BM2 cells. The red arrow marked a distinct 55-kDa band enriched in biotin-labeled tRF-1^{ArgACG} group compared to antisense. **(B)** The top 10 candidate

binding proteins identified by mass spectrometry analysis. **(C)** Western blot analysis showing specific enrichment of ALKBH5 in tRF-1^{ArgACG} RNA pull-down products from HepG2 and HCCLM3 cell lysates. Antisense probes were used as negative controls. **(D)** RIP assays were performed using anti-ALKBH5 or control IgG antibodies in HepG2 and HCCLM3 cells. tRF-qPCR assays revealed significant enrichment of tRF-1^{ArgACG} in ALKBH5-associated complexes compared to IgG controls. **(E)** Subcellular co-localization of tRF-1^{ArgACG} and ALKBH5 in HepG2 and HCCLM3 cells visualized by combined FISH and IF staining. Nuclei were counterstained with DAPI (scale bars, 25 μm). **(F)** Demethylase activity and m6A dot blot assays were performed to assess global demethylase activity and m6A levels in HepG2 and HCCLM3 cells with tRF-1^{ArgACG} overexpression. Methylene blue staining was used as a loading control. **(G)** RNA pull-down followed by Western blot analysis of ALKBH5 binding to wild-type tRF-1^{ArgACG} or the indicated U3A, U16A, and U3A/U16A mutants in HepG2 and HCCLM3 cells. Antisense RNA was used as a negative control. **(H)** Demethylase activity and m6A dot blot assays assessing the effects of the indicated treatments on ALKBH5 demethylase activity and global m6A levels in HepG2 and HCCLM3 cells. Methylene blue staining was used as a loading control. **(I)** RT-qPCR analysis of ALKBH5 and INPP4B mRNA levels, together with Western blot analysis of ALKBH5 and INPP4B and m6A dot blot assays, in HepG2 and HCCLM3 cells following tRF-1^{ArgACG} overexpression with or without ALKBH5 silencing. Methylene blue staining was used as a loading control. **(J)** Representative IHC staining images and quantification of ALKBH5 expression in para-tumor tissues (n=45), primary HCC tissues without bone metastasis (n=45), primary HCC tissues with bone metastasis (n=29), and bone-metastatic lesions (n=21) (scale bars, 50 μm). **(K)** Kaplan-Meier analysis of OS in HCC patients stratified into high (n=42) and low (n=42) ALKBH5 expression groups using the cohort-specific median staining score of 5.660 as the cut-off (n=84; HR = 2.268, 95% CI: 1.280–4.02; log-rank *P* = 0.0011). Data represent mean ± SD. ***P*< 0.01; ****P*< 0.001. ns, not significant.

Subsequently, blockade experiments demonstrated that ALKBH5 silencing rescued tRF-1^{ArgACG}-mediated suppression of INPP4B mRNA and protein in HepG2 and HCCLM3 cells **(Fig. 6I)**, supporting the requirement of ALKBH5 for tRF-1^{ArgACG}-mediated INPP4B suppression. Clinically, IHC revealed higher ALKBH5 protein levels in bone metastasis lesions (n=21) compared to primary HCC with bone metastasis (n=29), primary HCC without bone metastasis (n=45), or para-tumor liver tissues (n=45) **(Fig. 6J)**. Pearson correlation analysis indicated that ALKBH5 expression was positively correlated with tRF-1^{ArgACG} levels (n=21, *P*=0.0219; **Fig. S13H**) and negatively correlated with INPP4B levels (n=21, *P*=0.0418; **Fig. S13I**) in HCC bone-metastatic lesions. TCGA data showed elevated ALKBH5 expression in HCC tumors (n = 371) compared with normal liver tissues (n = 50) **(Fig. S13J)**. Kaplan-Meier survival analysis of HCC patients revealed that higher ALKBH5 expression was associated with significantly poorer OS both in the combined public datasets (n = 500; Log-rank *P* = 0.025; **Fig. S13K**) and in our cohort (n = 84; Log-rank *P* = 0.0011; **Fig. 6K**), whereas no significant association was observed with BMFS (n = 29; Log-rank P = 0.07255; **Fig. S13L**). Collectively, tRF-1^{ArgACG} suppresses INPP4B by enhancing the demethylase activity of ALKBH5.

ALKBH5 destabilizes INPP4B mRNA in an m6A-YTHDF2-dependent manner

To further elucidate the mechanism by which ALKBH5 modulates INPP4B, we knocked down ALKBH5 in HCCLM3-BM2 cells using two independent shRNAs. ALKBH5 knockdown significantly increased INPP4B mRNA and protein levels, with ALKBH5 KD1 showing greater knockdown efficiency **(Fig. 7A)**. Consistent with this, m6A dot blot analysis showed that ALKBH5 knockdown increased global m6A levels **(Fig. 7A)**. Treatment with the ALKBH5 inhibitor IOX1, which suppresses its demethylase activity, caused a dose-dependent increase in INPP4B mRNA and protein in HCCLM3-BM2 cells **(Fig. 7B)**. Overexpression of wild-type (WT) ALKBH5 reduced m6A levels and suppressed INPP4B mRNA and protein expression in HepG2 and HCCLM3 cells **(Fig. 7C-D)**. In contrast, overexpression of the catalytically inactive ALKBH5 H204A mutant had no significant effect on INPP4B expression **(Fig. 7C-D)**, supporting m6A modification involvement in ALKBH5-mediated INPP4B regulation. MeRIP-qPCR confirmed that ALKBH5 knockdown or enzymatic inhibition enhanced INPP4B m6A modification in HCCLM3-BM2 cells **(Fig. 7E, S14A)**. Furthermore, WT ALKBH5, but not the mutant, attenuated m6A methylation on INPP4B mRNA **(Fig. 7F, S14B)**, identifying INPP4B as an ALKBH5 downstream target *via* m6A modification.

Given the established role of m6A modification in regulating mRNA turnover, we next examined whether ALKBH5 affected the stability of INPP4B mRNA. Assessing INPP4B mRNA levels at 0, 3, 6, 9, and 12 hours post-actinomycin D treatment revealed that IOX1 treatment or ALKBH5 knockdown prolonged INPP4B half-life in HCCLM3-BM2 cells **(Fig. 7G, S14C)**. Conversely, WT ALKBH5, but not the mutant, decreased INPP4B half-life in HepG2 and HCCLM3 cells **(Fig. 7H, S14D)**, indicating ALKBH5 promotes INPP4B mRNA degradation *via* m6A. Bioinformatics analysis using SRAMP identified six candidate m6A sites on INPP4B, including positions 423, 1201, 1297, 2070, 2112, and 2955 **(Fig. 7I)**. Dual-luciferase reporter assays in HCC cells showed that ALKBH5 suppression increased luminescence for WT and Mut1-4/6 constructs but not Mut5 (2112 site) in HCCLM3-BM2 cells **(Fig. 7J, S14E)**. Conversely, ALKBH5 overexpression suppressed reporter output in WT and Mut1-4/6 groups, while Mut5 activity remained unchanged **(Fig. 7K, S14F)**, establishing the INPP4B 2112 m6A site as the principal ALKBH5-responsive element. To identify the m6A reader mediating this regulation, we interrogated interactions between INPP4B mRNA and canonical readers, including the YTH family and IGF2BPs. RNA pull-down analysis showed preferential binding of YTHDF2 to the WT INPP4B RNA probe among the m6A readers examined **(Fig. 7L, S14G)**, which was confirmed by RIP-qPCR showing YTHDF2-specific enrichment of INPP4B mRNA **(Fig. 7M, S14H)**.

YTHDF2 loss reduced INPP4B expression in HepG2 and HCCLM3 cells **(Fig. S14I)**. Moreover, ALKBH5 inhibition prolonged INPP4B transcript half-life, an effect abrogated by concurrent YTHDF2 knockdown **(Fig. 7N)**. Collectively, these data demonstrate that ALKBH5 destabilizes INPP4B mRNA in an m6A-YTHDF2-dependent manner.

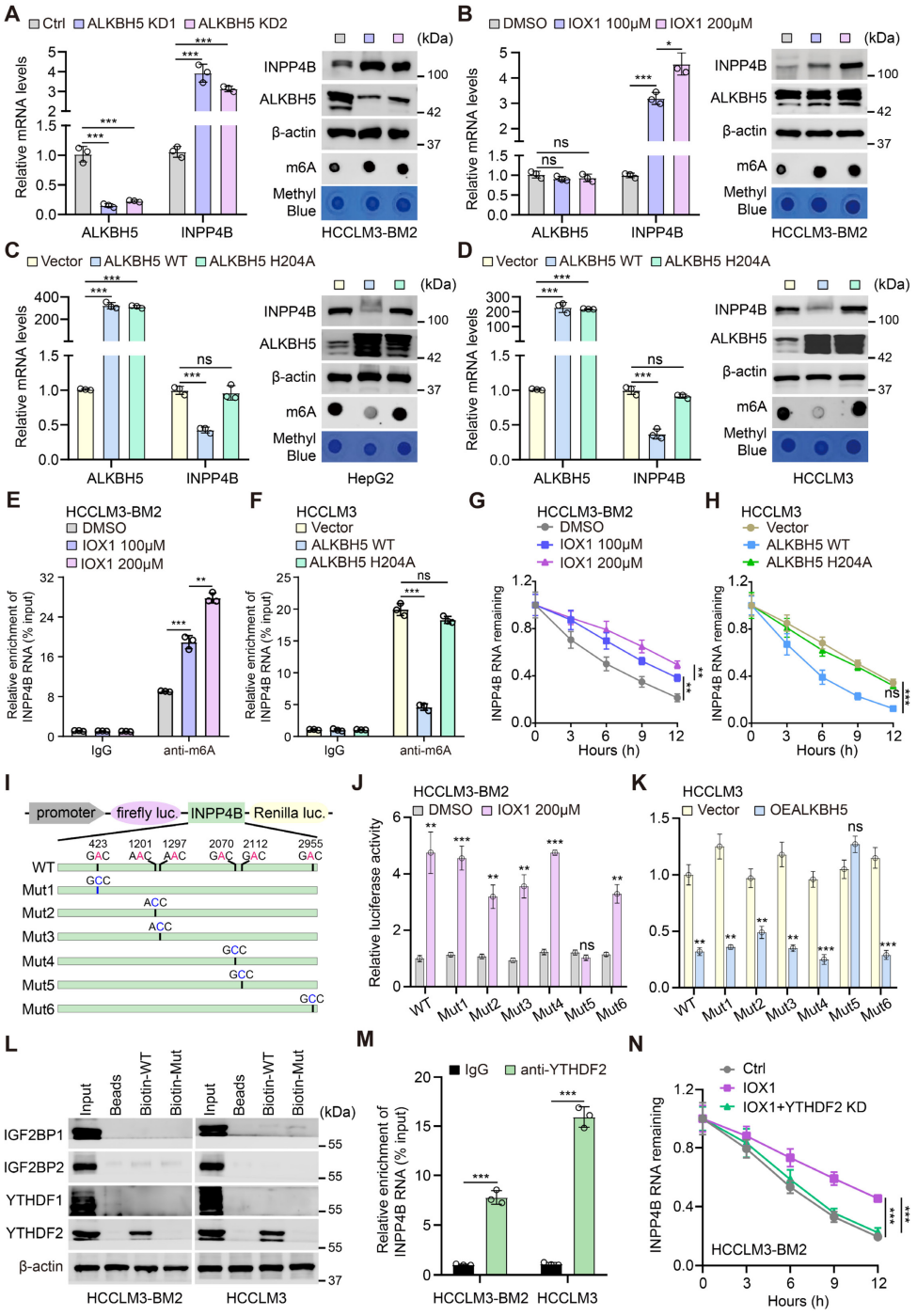


Figure 7. ALKBH5 destabilizes INPP4B mRNA in an m6A-YTHDF2-dependent manner. (A-B) ALKBH5 and INPP4B expression and m6A levels in HCCLM3-BM2 cells were assessed by RT-qPCR, Western blot, and m6A dot blot following ALKBH5 knockdown using two independent lentiviral shRNAs (A) or inhibition by IOX1 treatment (B). **(C-D)** RT-qPCR, Western blot, and m6A dot blot evaluated ALKBH5 and INPP4B expression and m6A levels in HepG2 (C) and HCCLM3 cells (D) transfected with wild-type (ALKBH5-WT) or mutant (ALKBH5-MUT) ALKBH5. **(E-F)** MeRIP-qPCR determined INPP4B mRNA m6A modification levels in HCCLM3-BM2 cells after ALKBH5 inhibition (E) and in HCCLM3 cells expressing ALKBH5-WT or ALKBH5-MUT (F). **(G-H)** INPP4B mRNA stability was measured *via* RT-qPCR in HCCLM3-BM2 cells with ALKBH5 inhibition (G) and in HCCLM3 cells expressing ALKBH5-WT or ALKBH5-MUT (H) post-actinomycin D treatment. **(I)** Schematic of luciferase reporters containing wild-type (WT) or m6A-site-mutated (Mut1-Mut6) INPP4B sequences. **(J)** Relative luciferase activity (Firefly/Renilla) in HCCLM3-BM2 cells co-treated with DMSO/IOX1 and INPP4B-WT or INPP4B-Mut reporters. **(K)** Relative luciferase activity in HCCLM3 cells co-transfected with Vector-NC/ALKBH5 plasmids and INPP4B-WT or INPP4B-Mut reporters. **(L)** RNA pull-down with biotinylated wild-type or m6A-site-mutated INPP4B probes in HCCLM3-BM2/HCCLM3 lysates, followed by Western blot for IGF2BP1, IGF2BP2, YTHDF1, and YTHDF2; input and beads-only were controls. **(M)** RIP using anti-YTHDF2 or IgG in HCCLM3-BM2/HCCLM3 cells showed significant INPP4B enrichment in YTHDF2 complexes by RT-qPCR. **(N)** INPP4B mRNA stability was assessed by RT-qPCR post-actinomycin D treatment in HCCLM3-BM2 cells treated with DMSO, IOX1, or IOX1 plus YTHDF2 knockdown. Data represent mean ± SD of triplicate experiments. **P*< 0.05; ***P*< 0.01; ****P*< 0.001. ns, not significant.

tRF-1^{ArgACG} disrupts bone homeostasis through modulating the ALKBH5/INPP4B/PI3K/AKT axis in HCC

Because INPP4B mRNA was identified as a demethylation target of ALKBH5 in HCC cells and its expression was repressed by ALKBH5, we investigated the role of ALKBH5 in regulating bone homeostasis and its potential mediation through INPP4B downregulation. CM from IOX1-treated or ALKBH5-knockdown HCCLM3-BM2 cells significantly reduced TRAP+ cells and impaired F-actin ring formation; these effects were reversed by INPP4B silencing **(Fig. S15A-D)**. Furthermore, CM from ALKBH5-suppressed HCCLM3-BM2 cells enhanced osteoblastogenesis, evidenced by increased ALP+ pre-OBs and ALP activity, and these effects were attenuated by INPP4B knockdown **(Fig. S15A-D)**. In addition, overexpression of ALKBH5 WT, but not the catalytically inactive H204A mutant, in HepG2 and HCCLM3 cells promoted CM-induced pre-OC fusion and maturation, and these effects were significantly attenuated by INPP4B restoration or PI3K inhibition (LY294002) **(Fig. S16A-B)**. Simultaneously, CM from ALKBH5 WT-overexpressing cells decreased pre-OB formation and ALP activity, which was rescued by INPP4B restoration or LY294002 treatment **(Fig. S16C-D)**. The H204A mutant CM had no significant effect, and further INPP4B elevation or LY294002 treatment under these conditions inhibited osteoclastogenesis and enhanced osteoblastogenesis **(Fig. S16A-D)**. Collectively, these results indicate that upregulation of ALKBH5 disrupts bone homeostasis by suppressing INPP4B *via* m6A demethylation.

We next investigated whether tRF-1^{ArgACG} disrupts bone homeostasis by modulating the ALKBH5/INPP4B/PI3K/AKT axis in HCC. As indicated, ALKBH5 inhibition substantially attenuated the osteolytic phenotype induced by tRF-1^{ArgACG} overexpression, and this attenuation could be counteracted by silencing INPP4B **(Fig. 8A-B)**. Notably, the PI3K inhibition using LY294002 further suppressed osteoclastogenesis while promoting osteoblastogenesis **(Fig. 8A-B)**. Furthermore, rescue experiments using the HCCLM3-BM2 co-culture system showed that ALKBH5 re-expression restored osteoclastogenic activity and suppressed osteogenic differentiation following tRF-1^{ArgACG} inhibition. These ALKBH5-mediated effects were reversed by IOX1, partially attenuated by INPP4B restoration, and further suppressed by LY294002 treatment **(Fig. S17A–B)**, suggesting that tRF-1^{ArgACG} disrupts bone homeostasis in HCC through modulating the ALKBH5/INPP4B/PI3K/AKT signaling axis *in vitro*.

To validate this mechanism *in vivo*, luciferase-labeled HCCLM3 cells expressing tRF-NC, tRF-1^{ArgACG}, or tRF-1^{ArgACG} with INPP4B knockdown were intracardially injected into nude mice, followed by treatment with IOX1 and/or LY294002 **(Fig. S17C)**. tRF-1^{ArgACG} overexpression markedly increased bone metastatic burden and shortened BMFS. IOX1 suppressed these effects, whereas INPP4B knockdown partially reversed its protective activity. Combined IOX1 and LY294002 treatment produced the strongest inhibition of bone metastasis **(Fig. 8C–E)**. Micro-CT showed that tRF-1^{ArgACG} overexpression aggravated osteolytic destruction, as indicated by decreased BV/TV, Tb.N, and Tb.Th and increased Tb.Sp and BS/BV. These changes were attenuated by IOX1, partially restored by INPP4B knockdown, and further ameliorated by LY294002 **(Fig. 8C, F; Fig. S17E)**. Consistently, IOX1 reduced TRAP-positive osteoclasts and CTSK expression while restoring OCN expression; INPP4B knockdown weakened these effects, whereas LY294002 further preserved bone homeostasis **(Fig. 8C, F; Fig. S17D–E)**. Collectively, these data underscore that tRF-1^{ArgACG} disrupts bone homeostasis in HCC through modulating the ALKBH5/INPP4B/PI3K/AKT signaling axis and implicate IOX1 and LY294002 as a promising therapeutic approach against HCC bone metastasis.

Discussion

HCC bone metastasis represents a complex pathophysiological cascade involving primary tumor cell dissemination, survival adaptation, bone tropism, and osteolytic remodeling, with bone homing and skeletal destruction constituting its hallmark pathological stages [1, 6]. During homing, HCC cells coordinate chemotaxis, adhesion, niche colonization, and proliferation *via* aberrant effector expression, while post-metastatic cells disrupt osteoblast-osteoclast homeostasis by secreting osteomimetic cytokines, thereby establishing a self-sustaining feedback cycle that intensifies OCs differentiation and bone resorption [9, 56]. Despite the identification of numerous therapeutic targets within this multi-step process, current clinical interventions remain restricted to bone-modifying agents lacking specificity, and no validated diagnostic biomarkers or pathway-targeted therapies have been established [57]. Deciphering the regulatory networks governing bone tropism and osteolytic progression, alongside their mechanistic underpinnings, remains a pivotal challenge for advancing HCC bone metastasis precision treatment [3, 7]. While tRFs play critical roles in malignancy initiation and progression, including HCC, their function in HCC bone metastasis remains poorly defined. In this study, we found that tRF-1^{ArgACG} was enriched in HCC bone-metastatic tissues

and cells and was associated with shorter BMFS. tRF-1^{ArgACG} overexpression promoted HCC cell bone homing, facilitated metastatic niche formation, and exacerbated skeletal-related events by disrupting bone homeostasis. Mechanistically, tRF-1^{ArgACG} promoted HCC bone metastasis by interacting with ALKBH5, enhancing its demethylase activity, leading to INPP4B mRNA destabilization and consequent activation of the PI3K/AKT signaling axis.

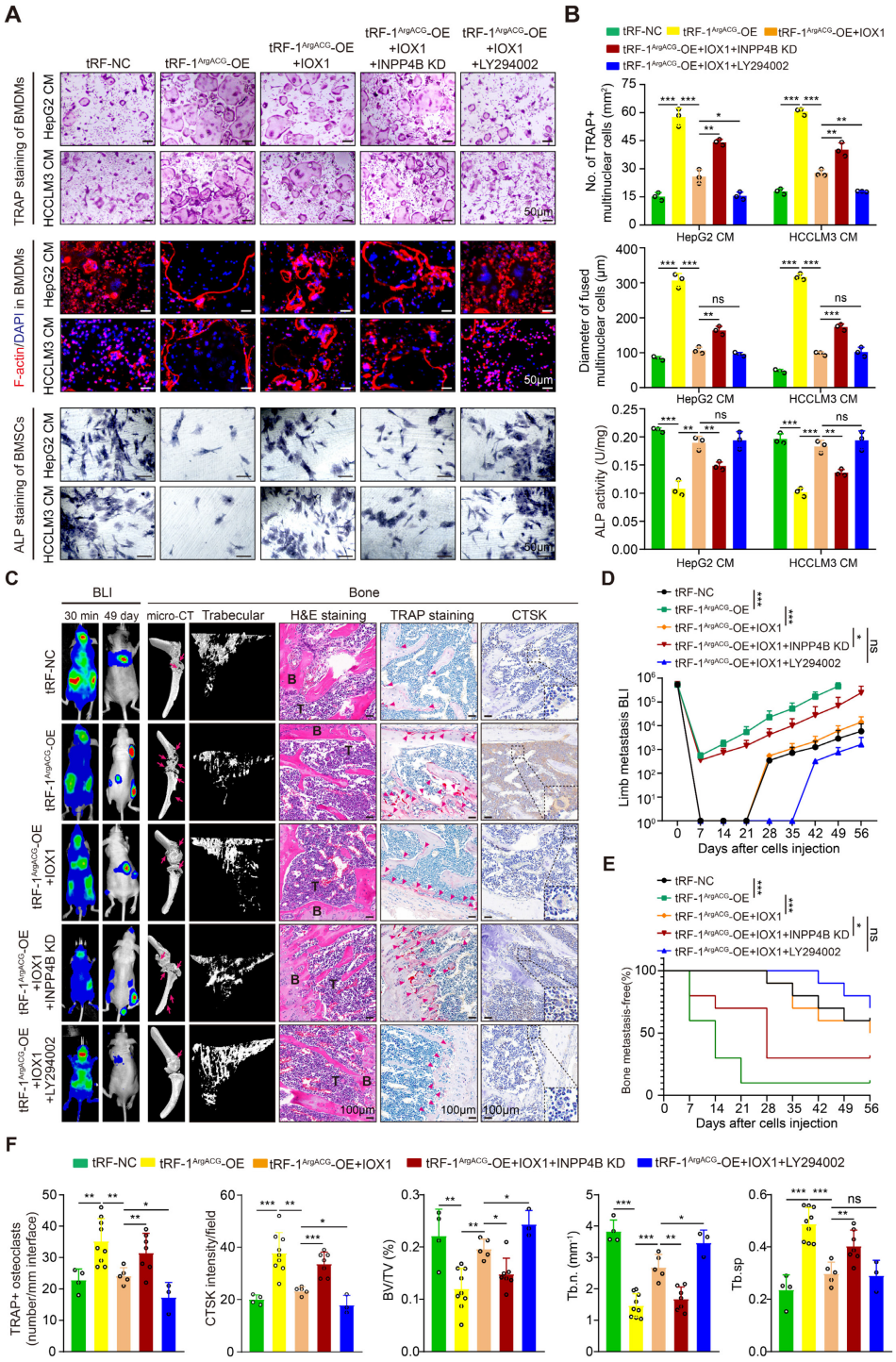


Figure 8. tRF-1^{ArgACG} disrupts bone homeostasis through modulating the ALKBH5/INPP4B/PI3K/AKT axis in HCC. (A-B) HepG2 (top) and HCCLM3 (bottom) cells were treated with tRF-NC, tRF-1^{ArgACG}, tRF-1^{ArgACG} co-treated with IOX1, tRF-1^{ArgACG} co-treated with IOX1 following silencing INPP4B, and tRF-1^{ArgACG} co-treated with IOX1 following LY294002 treatment. TRAP staining, F-actin ring formation and ALP staining assays were performed to evaluate osteoclastogenesis and osteoblastogenesis differences in the indicated HCC CM (scale bars, 50 μm). Representative images (A) and quantification (B) are shown. **(C)** Representative BLI images at 30 min and 49 days after intracardiac inoculation, together with micro-CT, trabecular bone reconstruction, H&E, TRAP, and CTSK staining of bone lesions from the indicated groups (n=10 successfully inoculated mice per group). B, bone; T, tumor. Scale bars, 100 μm. **(D)** Longitudinal quantification of limb metastatic BLI signals in the indicated experimental groups following intracardiac injection. **(E)** Kaplan-Meier curves showing BMFS in the indicated experimental groups. **(F)** Quantification of TRAP+ OCs, CTSK staining intensity, BV/TV, Tb.N, and Tb.Sp in bone lesions from the indicated groups. Data represent mean ± SD. *P< 0.05; **P< 0.01; ***P< 0.001. ns, not significant.

Emerging evidence underscores tRFs as pivotal regulators in HCC pathogenesis and metastatic dissemination, with dual roles as molecular biomarkers and therapeutic targets [22]. Zhou *et al*. identified Gly-tRF as an oncogenic driver mechanistically linked to liver cancer stem cell properties and epithelial-mesenchymal transition (EMT) *via* NDFIP2/AKT axis suppression [58]. Similarly, Liu *et al*. demonstrated 5'tRF-Gly overexpression in HCC, directly targeting CEACAM1 to drive oncogenic phenotypes including proliferation, invasion, and EMT [59]. Serum tRF-Gln-TTG-006 exhibited superior diagnostic accuracy in discriminating HCC from healthy controls, supporting its utility as a non-invasive biomarker [60]. Our investigation revealed tRF-1^{ArgACG} upregulation in bone-metastatic HCC, correlating with adverse clinical outcomes. Importantly, we demonstrated a significant elevation of serum tRF-1^{ArgACG} levels in HCC patients with osseous metastasis compared with those without bone metastasis. This association remained evident after excluding patients with concomitant extraosseous metastases. Circulating tRF-1^{ArgACG} levels were positively correlated with CTX but not P1NP, further supporting its association with osteolytic bone involvement. Notably, tRF-1^{ArgACG} expression was not significantly associated with OS, suggesting a closer relationship with bone metastatic progression than with overall prognosis in HCC. These findings support the potential of circulating tRF-1^{ArgACG} as a bone metastasis-associated biomarker in HCC. Functionally, tRF-1^{ArgACG} orchestrated bone niche remodeling through dual modulation of osteoclastogenesis activation and osteoblastogenesis inhibition, disrupting bone homeostasis to establish a pro-tumorigenic microenvironment. Our experimental strategy was guided by established HCC bone-metastasis models. HCCLM3 retains skeletal metastatic capacity despite its prominent pulmonary metastatic potential, and serial intracardiac selection has been successfully used to generate HCC derivatives with enhanced bone-metastatic competence [2, 4, 61]. We therefore used intracardiac inoculation to establish and characterize HCCLM3-BM1/BM2, which exhibited enhanced skeletal colonization and osteolytic remodeling while retaining the same parental background. Using this system, we further found that tRF-1^{ArgACG} promoted skeletal metastasis and osteolysis *in vivo*. Interestingly, both skeletal selection and tRF-1^{ArgACG} modulation were accompanied by changes in pulmonary metastatic burden **(Fig. S18)**, which were further supported by altered migration and adhesion toward Beas2B cells and changes in lung metastasis-associated factors, including ANGPTL4 and CXCL1 **(Fig. S19)**. These findings suggest that enhanced skeletal metastatic competence may be accompanied by altered interactions with the pulmonary microenvironment. However, the mechanisms underlying this pulmonary phenotype remain unresolved, and our data do not establish a reciprocal bone–lung metastatic switch.

While the mechanistic landscape of tRFs remains incompletely defined, accumulating evidence supports their roles in translational regulation, miRNA-like activity, and epigenetic crosstalk. For instance, CU1276 regulates B-cell lymphoma progression *via* RPA1 targeting [62], while 5'-tRF-GlyGCC enhances FTO activity to suppress autophagy in breast cancer [37]. Our study revealed that tRF-1^{ArgACG} directly interacted with ALKBH5 to modulate its demethylase activity without altering protein levels, resulting in global m6A reduction. Mutational analyses further showed that U16 contributed to tRF-1^{ArgACG}-ALKBH5 binding, with U16A and U3A/U16A mutations markedly impairing ALKBH5 binding and largely abolishing the tRF-induced increase in demethylase activity. Mechanistically, this tRF-mediated ALKBH5 activation destabilized INPP4B mRNA in an m6A-YTHDF2-dependent manner, thereby derepressing the PI3K/AKT axis to promote HCC bone metastasis. Emerging evidence highlights ALKBH5 as a dynamically regulated m6A demethylase with context-dependent oncogenic or tumor-suppressive functions across cancers [36, 63]. You *et al*. demonstrated that ALKBH5 overexpression in HCC correlated with poor clinical outcomes, mechanistically driving HCC progression via the ALKBH5/MAP3K8 axis [34]. Our findings revealed that ALKBH5 was progressively elevated in HCC tissues with bone metastatic involvement and bone metastatic lesions, and its elevation substantially enhanced osteolytic activity in HCC. However, this observation differs from Han SQ's report, where bone metastasis-derived exosomal miR-3190 suppresses ALKBH5 expression to exacerbate HCC metastasis [33]. These divergent findings highlight the critical role of m6A methylation in HCC bone metastasis but also underscore the complexity of ALKBH5 regulation in HCC bone metastasis, suggesting that tissue microenvironment-specific epigenetic rewiring governs its functional dichotomy in metastatic progression.

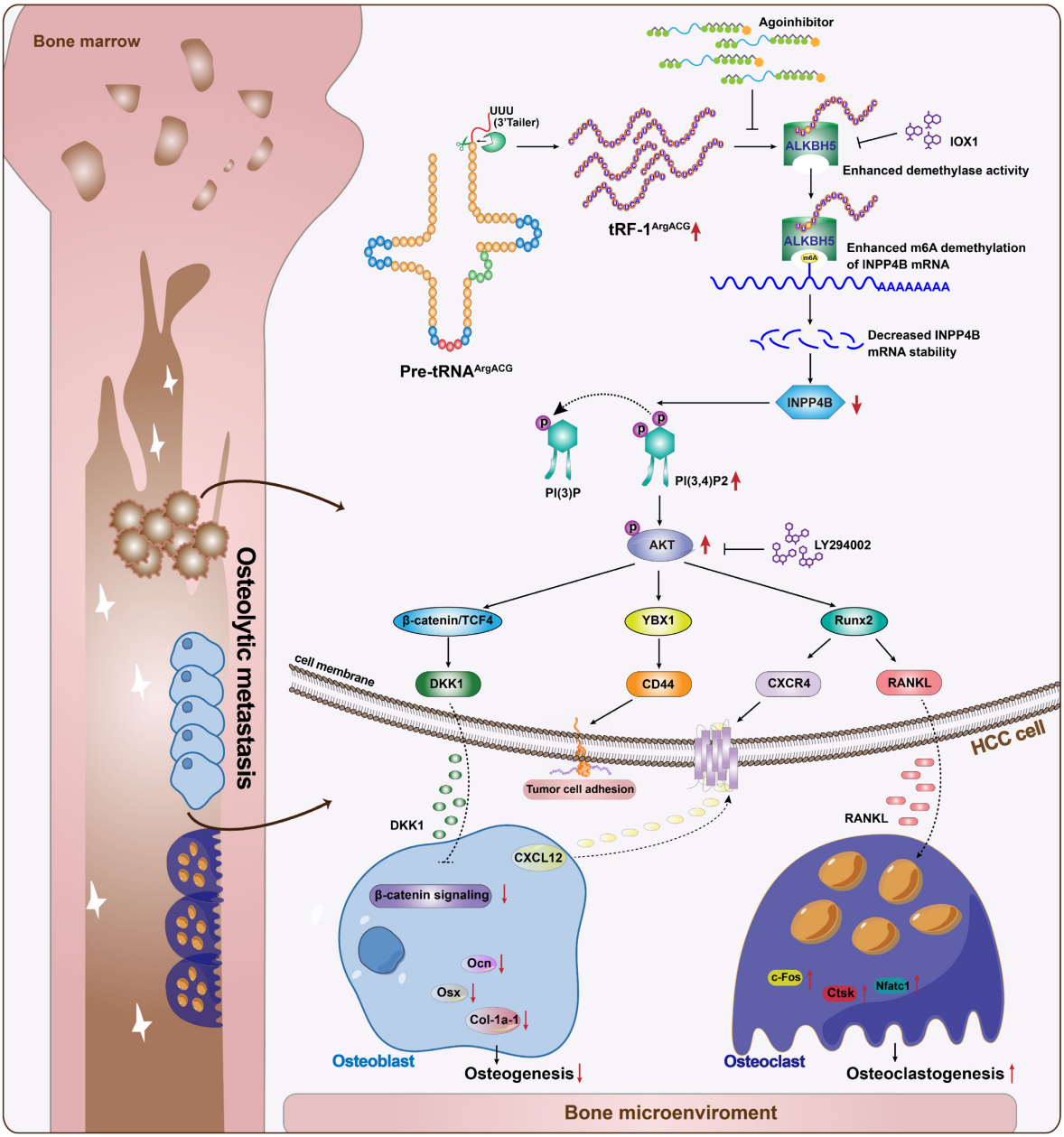


Figure 9. tRNA-derived fragment tRF-1^{ArgACG} drives HCC osteolytic bone metastasis via ALKBH5-mediated INPP4B destabilization and PI3K/AKT activation. tRF-1^{ArgACG}, derived from pre-tRNA^{ArgACG}, is significantly enriched in HCC bone-metastatic cells. tRF-1^{ArgACG} interacts with ALKBH5 to enhance its demethylase activity, thereby promoting m6A demethylation and destabilization of INPP4B mRNA in an m6A-YTHDF2-dependent manner and consequently activating the PI3K/AKT signaling axis. Downstream PI3K/AKT signaling engages β-catenin/TCF4, YBX1, and RUNX2 to regulate DKK1, CD44, CXCR4, and RANKL, respectively. These signaling branches promote HCC cell recruitment and adhesion within the bone microenvironment, enhance osteoclastogenesis, and suppress osteoblastogenesis, thereby facilitating osteolytic bone metastasis. Critically, the pro-metastatic effects driven by tRF-1^{ArgACG} overexpression were effectively reversed through targeted inhibition of tRF-1^{ArgACG}, ALKBH5 suppression, or pharmacologic blockade of the PI3K/AKT pathway using LY294002. These findings identify tRF-1^{ArgACG} as a key regulator of HCC bone metastasis pathogenesis and highlight its therapeutic potential for targeting osteolytic metastasis.

INPP4B, a phosphatase regulating PI3K/AKT signaling, emerges as a critical regulator of malignancy across cancers [39]. In triple-negative breast cancer (TNBC), INPP4B loss enhances PI3K/ERK signaling by prolonging EGFR/MET recycling, driving progression, and sensitizing cells to PI3K/MEK inhibitors [64]. Herein, INPP4B suppressed HCC bone metastasis under tRF-1^{ArgACG}/ALKBH5 axis modulation, promoting osteoblast differentiation while inhibiting osteoclastogenesis, consistent with prior observations [65]. Emerging studies underscore the PI3K/AKT signaling pathway as a pivotal regulator of bone metastasis, exemplified by KMT2B-EGF axis-driven cervical cancer bone metastasis *via* PI3K/AKT activation [66] and bone sialoprotein-mediated lung cancer osteolysis through this pathway [67]. Our findings revealed that INPP4B suppression activated PI3K/AKT signaling, mechanistically linking the tRF-1^{ArgACG}/ALKBH5 axis to HCC bone metastasis

progression. Downstream, PI3K/AKT activation engaged distinct transcriptional programs: RUNX2 promoted CXCR4 and RANKL expression, facilitating skeletal recruitment and osteoclastogenesis; YBX1 enhanced CD44 transcription, potentially contributing to tumor-cell adhesion within the bone niche; and β-catenin/TCF4 induced DKK1, thereby suppressing osteoblast differentiation. This aligned with prior evidence identifying INPP4B as a negative regulator of osteoclast differentiation through PI3K/NFATc1 modulation and as a genetic determinant of bone homeostasis [65]. Critically, pharmacological PI3K/AKT inhibition using LY294002 attenuated tRF-1^{ArgACG}-induced HCC bone metastasis, reinforcing its therapeutic relevance. These results collectively position that INPP4B/PI3K/AKT signaling controls bone homeostasis and offers insights into therapeutic targets in HCC bone metastasis pathogenesis.

Several limitations should be acknowledged. First, our intracardiac and intratibial models primarily address post-dissemination skeletal colonization and tumor–bone interactions and do not recapitulate the complete spontaneous metastatic cascade from primary HCC. Moreover, although changes in pulmonary metastatic behavior accompanied skeletal selection and tRF-1^{ArgACG} modulation, their mechanistic relationship with metastatic organotropism remains to be clarified. Second, although our mutational analyses identified U16 as an important nucleotide for tRF-1^{ArgACG}-ALKBH5 binding and demethylase activation, the structural basis by which this interaction modulates ALKBH5 activity remains unresolved and requires further structural and biochemical investigation. Third, the clinical analyses were based on relatively small, single-center cohorts, particularly for BMFS and metastasis-restricted subgroup analyses. Larger independent, multicenter cohorts are therefore required to validate the association between circulating tRF-1^{ArgACG} and HCC bone metastasis and determine its clinical utility.

Conclusion

In conclusion, we establish that tRF-1^{ArgACG}, derived from pre-tRNA^{ArgACG}, is significantly enriched in HCC bone-metastatic cells and tissues. tRF-1^{ArgACG} interacts with ALKBH5 to enhance its demethylase activity, thereby destabilizing INPP4B mRNA in an m6A-YTHDF2-dependent manner and consequently activating the PI3K/AKT signaling axis. Downstream activation of RUNX2, YBX1, and β-catenin/TCF4 regulates the expression of CXCR4, RANKL, CD44, and DKK1, respectively, promoting HCC cell recruitment and adaptation to the bone microenvironment while enhancing osteoclastogenesis and suppressing osteoblast differentiation. Critically, the pro-metastatic effects driven by tRF-1^{ArgACG} overexpression were effectively reversed through targeted inhibition of tRF-1^{ArgACG}, ALKBH5 suppression, or pharmacologic blockade of the PI3K/AKT pathway using LY294002 **(Fig. 9)**. These findings identify tRF-1^{ArgACG} as a key regulator of HCC bone metastasis pathogenesis and highlight its therapeutic potential for targeting osteolytic metastasis.

Supplementary Material

Supplementary figures and methods.
https://www.ijbs.com/v23p0182s1.pdf
Supplementary table 1: clinical information of HCC patients. https://www.ijbs.com/v23p0182s2.xlsx
Supplementary table 2: characteristics of HCC patients. https://www.ijbs.com/v23p0182s3.pdf
Supplementary table 3: tRF primers, shRNAs, antibodies. https://www.ijbs.com/v23p0182s4.xlsx
Supplementary table 4: metastatic distributions in individual mice.
https://www.ijbs.com/v23p0182s5.xlsx
Supplementary table 5: differentially expressed tRFs.
https://www.ijbs.com/v23p0182s6.xlsx
Supplementary table 6: RNA-seq.
https://www.ijbs.com/v23p0182s7.xlsx
Supplementary table 7: prediction of potential target genes by KangChen Biotech Inc.
https://www.ijbs.com/v23p0182s8.xlsx
Supplementary table 8: tRF interacting proteins.
https://www.ijbs.com/v23p0182s9.xlsx

Acknowledgements

We are grateful to the Tianjin Medical University Cancer Institute and Hospital's Department of Bone and Soft Tissue Tumors for providing us with the experimental platform.

Funding

This study was funded by the National Natural Science Foundation of China (Grant No. 82303076 and Grant No. 82472905), State Key Laboratory of Druggability Evaluation and Systematic Translational Medicine (Grant No. QZ23-10), Tianjin Health Research Project (Grant No. TJWJ2023QN016), and Science & Technology Development Fund of Tianjin Education Commission for Higher Education (Grant No. 2022KJ225).

Ethics approval and consent to participate

The Tianjin Medical University Animal Care and Use Committee approved all procedures involving animals.

Author contributions

Guowen Wang, Bowen Liu and Yafei Wang conceptualized and designed the study. Jinyan Feng, Long Chen and Xianfu Wei carried out the experiments and drafted the manuscript. Houzhi Yang, Xiuxin Han, Qian Li and Xin Chen gathered clinical data and conducted the clinical data analysis. Qingqian Zhao and Chao Zhang performed bioinformatics and statistical analyses. Houzhi Yang, and Qingqian Zhao critically reviewed and revised the manuscript. Jinyan Feng, Long Chen and Xianfu Wei were responsible for the design and finalization of tables and figures. All authors read and approved the final manuscript.

Competing Interests

The authors have declared that no competing interests exist. All authors consented to publication.

References

1. Harding JJ, Abu-Zeinah G, Chou JF, Owen DH, Ly M, Lowery MA, et al. Frequency, Morbidity, and Mortality of Bone Metastases in Advanced Hepatocellular Carcinoma. J Natl Compr Canc Netw. 2018; 16: 50-8.
2. Huang Z, Chu L, Liang J, Tan X, Wang Y, Wen J, et al. H19 Promotes HCC Bone Metastasis Through Reducing Osteoprotegerin Expression in a Protein Phosphatase 1 Catalytic Subunit Alpha/p38 Mitogen-Activated Protein Kinase-Dependent Manner and Sponging microRNA 200b-3p. Hepatology. 2021; 74: 214-32.
3. Yuan X, Zhuang M, Zhu X, Cheng D, Liu J, Sun D, et al. Emerging Perspectives of Bone Metastasis in Hepatocellular Carcinoma. Front Oncol. 2022; 12: 943866.
4. Zhang S, Xu Y, Xie C, Ren L, Wu G, Yang M, et al. RNF219/alpha-Catenin/LGALS3 Axis Promotes Hepatocellular Carcinoma Bone Metastasis and Associated Skeletal Complications. Adv Sci (Weinh). 2021; 8: 2001961.
5. Zhang S, Liao X, Chen S, Qian W, Li M, Xu Y, et al. Large Oncosome-Loaded VAPA Promotes Bone-Tropic Metastasis of Hepatocellular Carcinoma Via Formation of Osteoclastic Pre-Metastatic Niche. Adv Sci (Weinh). 2022; 9: e2201974.
6. Doreille A, N'Kontchou G, Halimi A, Bouhafs F, Coderc E, Sellier N, et al. Percutaneous treatment of extrahepatic recurrence of hepatocellular carcinoma. Diagn Interv Imaging. 2016; 97: 1117-23.
7. Huang Z, Wen J, Wang Y, Han S, Li Z, Hu X, et al. Bone metastasis of hepatocellular carcinoma: facts and hopes from clinical and translational perspectives. Front Med. 2022; 16: 551-73.
8. Lasagna A, Cuzzocrea F, Maccario G, Mahagna A, Sacchi P, U Mondelli M. Bone metastases and hepatocellular carcinoma: some food for thought. Future Oncol. 2021; 17: 3777-80.
9. Muscarella AM, Aguirre S, Hao X, Waldvogel SM, Zhang XH. Exploiting bone niches: progression of disseminated tumor cells to metastasis. J Clin Invest. 2021; 131.
10. Ozer M, Goksu SY, Lin RY, Ayasun R, Kahramangil D, Rogers SC, et al. Effects of Clinical and Tumor Characteristics on Survival in Patients with Hepatocellular Carcinoma with Bone Metastasis. J Hepatocell Carcinoma. 2023; 10: 1129-41.
11. Wang M, Xia F, Wei Y, Wei X. Molecular mechanisms and clinical management of cancer bone metastasis. Bone Research. 2020; 8(1):30.
12. Mundy GR. Metastasis to bone: causes, consequences and therapeutic opportunities. Nat Rev Cancer. 2002; 2: 584-93.
13. Sharma G, Pothuraju R, Kanchan RK, Batra SK, Siddiqui JA. Chemokines network in bone metastasis: Vital regulators of seeding and soiling. Seminars in Cancer Biology. 2022; 86: 457-72.
14. Coleman RE, Croucher PI, Padhani AR, Clezardin P, Chow E, Fallon M, et al. Bone metastases. Nat Rev Dis Primers. 2020; 6: 83.
15. Yang H, Yu Z, Ji S, Huo Q, Yan J, Gao Y, et al. Targeting bone microenvironments for treatment and early detection of cancer bone metastatic niches. Journal of Controlled Release. 2022; 341: 443-56.
16. Clézardin P, Coleman R, Puppo M, Ottewell P, Bonnelye E, Paycha F, et al. Bone metastasis: mechanisms, therapies, and biomarkers. Physiological Reviews. 2021; 101: 797-855.
17. Wang Y, Wang C, Xia M, Tian Z, Zhou J, Berger JM, et al. Engineering small-molecule and protein drugs for targeting bone tumors. Molecular Therapy. 2024; 32: 1219-37.
18. Ren D, Mo Y, Yang M, Wang D, Wang Y, Yan Q, et al. Emerging roles of tRNA in cancer. Cancer Lett. 2023; 563: 216170.
19. Yu X, Xie Y, Zhang S, Song X, Xiao B, Yan Z. tRNA-derived fragments: Mechanisms underlying their regulation of gene expression and potential applications as therapeutic targets in cancers and virus infections. Theranostics. 2021; 11: 461-9.
20. Liu B, Cao J, Wang X, Guo C, Liu Y, Wang T. Deciphering the tRNA-derived small RNAs: origin, development, and future. Cell Death Dis. 2021; 13: 24.
21. Magee R, Rigoutsos I. On the expanding roles of tRNA fragments in modulating cell behavior. Nucleic Acids Res. 2020; 48: 9433-48.
22. Gupta T, Malkin MG, Huang S. tRNA Function and Dysregulation in Cancer. Front Cell Dev Biol. 2022; 10: 886642.
23. Lu J, Zhu P, Zhang X, Zeng L, Xu B, Zhou P. tRNA-derived fragments: Unveiling new roles and molecular mechanisms in cancer progression. Int J Cancer. 2024; 155: 1347-60.
24. Yang W, Gao K, Qian Y, Huang Y, Xiang Q, Chen C, et al. A novel tRNA-derived fragment AS-tDR-007333 promotes the malignancy of NSCLC via the HSPB1/MED29 and ELK4/MED29 axes. J Hematol Oncol. 2022; 15: 53.
25. Zhou M, He X, Zhang J, Mei C, Zhong B, Ou C. tRNA-derived small RNAs in human cancers: roles, mechanisms, and clinical application. Mol Cancer. 2024; 23: 76.
26. Schorn AJ, Gutbrod MJ, LeBlanc C, Martienssen R. LTR-Retrotransposon Control by tRNA-Derived Small RNAs. Cell. 2017; 170: 61-71 e11.
27. Kuscu C, Kumar P, Kiran M, Su Z, Malik A, Dutta A. tRNA fragments (tRFs) guide Ago to regulate gene expression post-transcriptionally in a Dicer-independent manner. RNA. 2018; 24: 1093-105.
28. Goodarzi H, Liu X, Nguyen HC, Zhang S, Fish L, Tavazoie SF. Endogenous tRNA-Derived Fragments Suppress Breast Cancer Progression via YBX1 Displacement. Cell. 2015; 161: 790-802.
29. Ivanov P, Emara MM, Villen J, Gygi SP, Anderson P. Angiogenin-induced tRNA fragments inhibit translation initiation. Mol Cell. 2011; 43: 613-23.
30. Jiang X, Liu B, Nie Z, Duan L, Xiong Q, Jin Z, et al. The role of m6A modification in the biological functions and diseases. Signal Transduct Target Ther. 2021; 6: 74.
31. Zhao Z, Meng J, Su R, Zhang J, Chen J, Ma X, et al. Epitranscriptomics in liver disease: Basic concepts and therapeutic potential. J Hepatol. 2020; 73: 664-79.
32. Chen Y, Zhao Y, Chen J, Peng C, Zhang Y, Tong R, et al. ALKBH5 suppresses malignancy of hepatocellular carcinoma via m(6)A-guided epigenetic inhibition of LYPD1. Mol Cancer. 2020; 19: 123.
33. Han S, Xue L, Wei Y, Yong T, Jia W, Qi Y, et al. Bone Lesion-Derived Extracellular Vesicles Fuel Prometastatic Cascades in Hepatocellular Carcinoma by Transferring ALKBH5-Targeting miR-3190-5p. Adv Sci (Weinh). 2023; 10: e2207080.
34. You Y, Wen D, Zeng L, Lu J, Xiao X, Chen Y, et al. ALKBH5/MAP3K8 axis regulates PD-L1+ macrophage infiltration and promotes hepatocellular carcinoma progression. Int J Biol Sci. 2022; 18: 5001-18.
35. Zhang H, Liu Y, Wang W, Liu F, Wang W, Su C, et al. ALKBH5-mediated m(6)A modification of lincRNA LINC02551 enhances the stability of DDX24 to promote hepatocellular carcinoma growth and metastasis. Cell Death Dis. 2022; 13: 926.
36. Qu J, Yan H, Hou Y, Cao W, Liu Y, Zhang E, et al. RNA demethylase ALKBH5 in cancer: from mechanisms to therapeutic potential. J Hematol Oncol. 2022; 15: 8.
37. Chen F, Song C, Meng F, Zhu Y, Chen X, Fang X, et al. 5'-tRF-GlyGCC promotes breast cancer metastasis by increasing fat mass and obesity-associated protein demethylase activity. Int J Biol Macromol. 2023; 226: 397-409.
38. Kofuji S, Kimura H, Nakanishi H, Nanjo H, Takasuga S, Liu H, et al. INPP4B Is a PtdIns(3,4,5)P3 Phosphatase That Can Act as a Tumor Suppressor. Cancer Discov. 2015; 5: 730-9.
39. Woolley JF, Dzneladze I, Salmena L. Phosphoinositide signaling in cancer: INPP4B Akt(s) out. Trends Mol Med. 2015; 21: 530-2.
40. Ferron M, Boudiffa M, Arsenault M, Rached M, Pata M, Giroux S, et al. Inositol polyphosphate 4-phosphatase B as a regulator of bone mass in mice and humans. Cell Metab. 2011; 14: 466-77.
41. Hinz N, Jucker M. AKT in Bone Metastasis of Solid Tumors: A Comprehensive Review. Cancers (Basel). 2021; 13(10):2287.
42. Song M, Bode AM, Dong Z, Lee MH. AKT as a Therapeutic Target for Cancer. Cancer Res. 2019; 79: 1019-31.
43. Cohen-Solal KA, Boregowda RK, Lasfar A. RUNX2 and the PI3K/AKT axis reciprocal activation as a driving force for tumor progression. Mol Cancer. 2015; 14: 137.
44. Mimeault M, Batra SK. Hypoxia-inducing factors as master regulators of stemness properties and altered metabolism of cancer- and metastasis-initiating cells. J Cell Mol Med. 2013; 17: 30-54.
45. Yuan G, Lian Z, Liu Q, Lin X, Xie D, Song F, et al. Phosphatidyl inositol 3-kinase (PI3K)-mTOR inhibitor PKI-402 inhibits breast cancer induced osteolysis. Cancer Lett. 2019; 443: 135-44.
46. Hou R, Wang YW, Liang HF, Zhang ZG, Liu ZM, Zhang BH, et al. Animal and cellular models of hepatocellular carcinoma bone metastasis: establishment and characterisation. J Cancer Res Clin Oncol. 2015; 141: 1931-43.
47. Hofbauer LC, Bozec A, Rauner M, Jakob F, Perner S, Pantel K. Novel approaches to target the microenvironment of bone metastasis. Nat Rev Clin Oncol. 2021; 18: 488-505.
48. Qiang YW, Barlogie B, Rudikoff S, Shaughnessy JD, Jr. Dkk1-induced inhibition of Wnt signaling in osteoblast differentiation is an underlying mechanism of bone loss in multiple myeloma. Bone. 2008; 42: 669-80.

49. Wu XB, Li Y, Schneider A, Yu W, Rajendren G, Iqbal J, et al. Impaired osteoblastic differentiation, reduced bone formation, and severe osteoporosis in noggin-overexpressing mice. J Clin Invest. 2003; 112: 924-34.
50. Matthijssens F, Sharma ND, Nysus M, Nickl CK, Kang H, Perez DR, et al. RUNX2 regulates leukemic cell metabolism and chemotaxis in high-risk T cell acute lymphoblastic leukemia. J Clin Invest. 2021; 131 (6):e141566.
51. Kitazawa R, Mori K, Yamaguchi A, Kondo T, Kitazawa S. Modulation of mouse RANKL gene expression by Runx2 and vitamin D3. J Cell Biochem. 2008; 105: 1289-97.
52. Pande S, Browne G, Padmanabhan S, Zaidi SK, Lian JB, van Wijnen AJ, et al. Oncogenic cooperation between PI3K/Akt signaling and transcription factor Runx2 promotes the invasive properties of metastatic breast cancer cells. J Cell Physiol. 2013; 228: 1784-92.
53. To K, Fotovati A, Reipas KM, Law JH, Hu K, Wang J, et al. Y-box binding protein-1 induces the expression of CD44 and CD49f leading to enhanced self-renewal, mammosphere growth, and drug resistance. Cancer Res. 2010; 70: 2840-51.
54. Niida A, Hiroko T, Kasai M, Furukawa Y, Nakamura Y, Suzuki Y, et al. DKK1, a negative regulator of Wnt signaling, is a target of the beta-catenin/TCF pathway. Oncogene. 2004; 23: 8520-6.
55. Song Y, Gao H, Pan Y, Gu Y, Sun W, Wang Y, et al. ALKBH5 Regulates Osteogenic Differentiation via the lncRNA/mRNA Complex. J Dent Res. 2024; 103: 1119-29.
56. Weilbaecher KN, Guise TA, McCauley LK. Cancer to bone: a fatal attraction. Nat Rev Cancer. 2011; 11: 411-25.
57. Satcher RL, Zhang XH. Evolving cancer-niche interactions and therapeutic targets during bone metastasis. Nat Rev Cancer. 2022; 22: 85-101.
58. Zhou Y, Hu J, Liu L, Yan M, Zhang Q, Song X, et al. Gly-tRF enhances LCSC-like properties and promotes HCC cells migration by targeting NDFIP2. Cancer Cell Int. 2021; 21: 502.
59. Liu D, Wu C, Wang J, Zhang L, Sun Z, Chen S, et al. Transfer RNA-derived fragment 5'tRF-Gly promotes the development of hepatocellular carcinoma by direct targeting of carcinoembryonic antigen-related cell adhesion molecule 1. Cancer Sci. 2022; 113: 3476-88.
60. Zhan S, Yang P, Zhou S, Xu Y, Xu R, Liang G, et al. Serum mitochondrial tsRNA serves as a novel biomarker for hepatocarcinoma diagnosis. Front Med. 2022; 16: 216-26.
61. Li Y, Tang Y, Ye L, Liu B, Liu K, Chen J, et al. Establishment of a hepatocellular carcinoma cell line with unique metastatic characteristics through *in vivo* selection and screening for metastasis-related genes through cDNA microarray. J Cancer Res Clin Oncol. 2003; 129: 43-51.
62. Maute RL, Schneider C, Sumazin P, Holmes A, Califano A, Basso K, et al. tRNA-derived microRNA modulates proliferation and the DNA damage response and is down-regulated in B cell lymphoma. Proc Natl Acad Sci U S A. 2013; 110: 1404-9.
63. Shen D, Wang B, Gao Y, Zhao L, Bi Y, Zhang J, et al. Detailed resume of RNA m(6)A demethylases. Acta Pharm Sin B. 2022; 12: 2193-205.
64. Liu H, Paddock MN, Wang H, Murphy CJ, Geck RC, Navarro AJ, et al. The INPP4B Tumor Suppressor Modulates EGFR Trafficking and Promotes Triple-Negative Breast Cancer. Cancer Discov. 2020; 10: 1226-39.
65. Vacher J. Inpp4b is a novel negative modulator of osteoclast differentiation and a prognostic locus for human osteoporosis. Ann N Y Acad Sci. 2013; 1280: 52-4.
66. Zhao D, Yuan H, Fang Y, Gao J, Li H, Li M, et al. Histone Methyltransferase KMT2B Promotes Metastasis and Angiogenesis of Cervical Cancer by Upregulating EGF Expression. Int J Biol Sci. 2023; 19: 34-49.
67. Chen WC, Chang AC, Tsai HC, Liu PI, Huang CL, Guo JH, et al. Bone sialoprotein promotes lung cancer osteolytic bone metastasis via MMP14-dependent mechanisms. Biochem Pharmacol. 2023; 211: 115540.